

Investigating the Electroweak Phase Transition with a Real Scalar Singlet at a Muon Collider

Mohamed Aboudonia,¹ Csaba Balazs,¹ Andreas Papaefstathiou² and Graham White³

¹*School of Physics and Astronomy, Monash University, Melbourne 3800 Victoria, Australia*

²*Department of Physics, Kennesaw State University, 830 Polytechnic Lane, Marietta, GA 30060, USA*

³*School of Physics and Astronomy, University of Southampton, Southampton SO17 1BJ, UK*

E-mail: mohamed.aboudonia@monash.edu, csaba.balazs@monash.edu,
apapaefs@kennesaw.edu, G.A.White@soton.ac.uk

ABSTRACT: A strong first-order electroweak phase transition (SFOEWPT) is essential for explaining baryogenesis, and for potentially generating observable gravitational waves. In the present study, we investigate the potential of a high-energy muon collider to examine the occurrence of SFOEWPT within the context of a Standard Model extended by a real scalar singlet (xSM). We present an analysis of all viable decay modes of a singlet-like scalar particle, in order to constrain the valid parameter space of SFOEWPT, which was extracted numerically at different renormalization scales to account for theoretical uncertainties. This allowed us to determine the sensitivity of a muon collider to the production and decay channels of new heavy scalar singlet-like particles that emerge in the xSM. Our findings demonstrate that a 3 TeV muon collider could directly probe the nature of electroweak symmetry breaking by efficiently detecting new scalar particles associated with a first-order electroweak phase transition through jet-rich final states, thus complementing the indirect constraints from gravitational wave experiments.

Keywords: Electroweak phase transition, real singlet extension

Contents

1	Introduction	1
2	Electroweak Phase Transition with a Scalar Singlet	3
2.1	First-Order Electroweak Phase Transition Parameter Space within the xSM	10
3	The Electroweak Phase Transition at Colliders	13
3.1	Direct Singlet Production at Colliders	13
3.2	Indirect Evidence: Modification of Higgs Boson Couplings	14
4	Constraints on the xSM at a Muon Collider	15
4.1	Event Generation	17
4.2	$4l$ Final States	18
4.3	$4q$ Final States	20
4.4	$2l2q$ Final States	22
4.5	$2\gamma 2q$ Final States	25
4.6	$2l2\nu_l$ Final states	27
4.7	$2q2\nu_l$ Final states	30
4.8	$l\nu_l 2q$ Final states	31
5	Results	33
6	Conclusions	37

1 Introduction

Several aspects of the current structure of the universe remain enigmatic, tracing their origins to the initial moments of its existence, when symmetry breaking resulted in the differentiation of the fundamental forces observed today. Electroweak symmetry breaking (EWSB) occurred approximately 10^{-11} s after Big Bang, leading to the generation of masses for most Standard Model (SM) particles, followed by chiral symmetry breaking ($\sim 10^{-3}$ s), which led to hadron confinement. Electroweak symmetry was spontaneously broken when the thermal evolution of the universe reached a state where the Higgs field's potential became unstable around its vanishing minimum, at the origin, leading to a transition towards another non-vanishing, “broken”, minimum that evolved at lower temperatures, a phenomenon referred to as the electroweak phase transition (EWPT) [1–7]. This transition could play the role of Sakharov’s third condition for explaining baryogenesis, i.e. the generation of the observed matter-antimatter asymmetry, if it was of the first-order type. Additionally, CP-violating processes that constitute Sakharov’s second condition would have to occur in thermal disequilibrium, in order to prevent the sphaleron wash-out of the

generated asymmetric baryon number (Sakharov’s first condition) [8–14]. Previous studies have shown that this sphaleron condition, which is quantitatively expressed as $\frac{E_{\text{sp}}(T_c)}{T_c} > 45$, can be translated into a relation between the theoretical parameters: $\frac{v(T_c)}{T_c} \geq 1$. This condition can only be satisfied if a first-order EWPT (FOEWPT) occurs [15, 16]. A FOEWPT is characterized by the existence of two degenerate minima that are separated by a barrier at some critical temperature T_c . In the SM, such behavior can only arise from the cubic term in the Higgs field, generated from thermal loop corrections, which is further suppressed by a mass-screening effect resulting from the IR-divergences from the massless Matsubara modes. Earlier studies have suggested that the SM can still produce a FOEWPT if thermal corrections with the leading contribution of the IR-divergent daisy diagrams are included [17]. However, subsequent studies demonstrated that this possibility disappears when the subleading terms of the daisy and superdaisy contributions are included, which shifts the SM phase transition more towards the second-order type [18, 19]. Currently, it is established that a large Higgs boson mass cannot allow for FOEWPT, therefore, at best, the SM EWPT can only be of crossover type when all non-perturbative corrections are included [20, 21]. Thus, to explain spontaneous symmetry breaking through a FOEWPT, additional degree(s) of freedom must be added to the SM to improve the sphaleron condition, primarily by strengthening the Higgs field’s vacuum expectation value through coupling with other scalar degrees of freedom.

Multiple extensions have been proposed in recent decades, including additional real scalars, complex scalars, Higgs doublets, and supersymmetric extensions [22–30]. The real gauge-singlet extension (xSM) is considered to be one of the simplest, yet promising, extensions to the Standard Model (SM) for several reasons. Primarily, it can enhance the sphaleron condition through direct correction to Higgs vacuum expectation value (vev) at the tree level. Additionally, it serves as a simplified model for more complex extensions, such as that of a complex singlet, or the Next-to-Minimal Supersymmetric Standard Model (NMSSM), in which multiple scalar fields exist with a substantial mass hierarchy. This hierarchy effectively isolates the heavier scalars from the electroweak symmetry breaking dynamics, with a contribution that is exponentially suppressed, resulting in only the lighter scalar being the effective scalar particle, which is adequately approximated by xSM [30]. Conversely, this scenario presents significant testing challenges, often referred to as the “nightmare scenario”, which renders it valuable for evaluating future colliders and assessing their capacity to make definitive statements regarding the nature of electroweak symmetry breaking. Consequently, a critical examination of xSM can effectively serve as a concurrent investigation of some of more complex extensions. For these reasons, this model has been extensively explored in previous works, including studies of its implications for the gravitational waves produced by real vacuum bubble dynamics, and its phenomenological consequences on the precision of the Higgs portal couplings at colliders [26, 27, 31–34].

While the nature of electroweak symmetry breaking is currently being explored at the Large Hadron Collider (LHC), it is also advantageous to examine its prospects in future collider facilities [26]. A high-energy muon collider can provide sufficient energy and integrated luminosity, to obtain information complementary to that of the LHC [35–

37]. In particular, the clean experimental environment of the muon collider will facilitate high-precision measurements in the Higgs sector. These measurements can potentially provide valuable information regarding the possible extensions of SM, which may enable us to elucidate the mechanism of electroweak symmetry breaking. Furthermore, the direct detection of an additional scalar at a muon collider will facilitate more comprehensive analyses of all potential decay modes due to the enhanced reconstruction capabilities of final state events, including those with invisible final states. Consequently, it is possible to optimize the search for a scalar in a muon collider by knowing its approximate mass. In the context of electroweak symmetry breaking, the mass of the scalar augmenting the strength of the phase transition is typically close to the electroweak scale, which is within the operational range of a muon collider. This characteristic renders the muon collider an ideal environment for discovering a new scalar particle associated with electroweak symmetry breaking. In this article, we present an analysis of the minimum sensitivity of a future muon collider to probe a real scalar singlet field that could mediate a strong FOEWPT. We focus on the kinematical region where the new scalar particle’s mass exceeds that of the SM Higgs boson mass, thereby allowing for decays into two Higgs bosons, consistent with current LHC constraints. Subsequently, by analyzing the decay channels, we identify the most promising avenues for investigation in a future muon collider.

The remainder of this paper is structured as follows: Section 2 aims to elucidate how the real singlet extension enhances the electroweak phase transition (EWPT) to be of a first-order type. Approximations were employed where appropriate to simplify calculations and highlight the primary features for pedagogical purposes. In addition, this section discusses the constraints utilized to identify the parameter space points that are consistent with FOEWPT. Section 3 addresses the direct and indirect verifications of xSM at colliders. Section 4 presents an analysis of the various channels of the new heavy scalar decay. Finally, Section 5 discusses the results and provides commentary on the subsequent steps of this investigation.

2 Electroweak Phase Transition with a Scalar Singlet

The most general renormalizable gauge-singlet scalar potential takes the form,

$$V(S) = \rho S + \frac{1}{2}\mu_s^2 S^2 + \frac{1}{4}\lambda_s S^4 + \frac{1}{3}\beta S^3. \quad (2.1)$$

The singlet scalar S can couple to the Higgs field H using the following terms,

$$V_{\text{int}} = \frac{1}{2}\alpha S(H^\dagger H) + \frac{1}{4}\lambda_{hs} S^2(H^\dagger H). \quad (2.2)$$

A \mathbb{Z}_2 -symmetric potential can be obtained directly by setting the parameters of the odd term to zero (i.e. $\alpha, \beta \rightarrow 0$). In this case, if the mass of the resulting new scalar exceeds half of the Higgs boson mass, it becomes challenging to detect at the colliders. This phenomenon is commonly referred to as the “nightmare scenario”. Nevertheless, in this study, we opted to keep these \mathbb{Z}_2 -asymmetric terms to maintain a more general representation that encompasses other types of challenging scenarios that induce some hard-to-reach regions of

the parameter space, where both the mixing angle and di-Higgs boson decays are minimal. In addition, these specific terms are crucial for facilitating a strong first-order EWPT, see e.g. [23]. The singlet term in the scalar field can be eliminated using shift symmetry, which only results in the redefinition of the remaining parameters, as demonstrated in previous studies [22, 38]. Consequently, the most general renormalizable representation of the real gauge-singlet extension of SM (xSM) is,

$$V(H, S) = -\frac{1}{2}\mu_h^2(H^\dagger H) + \frac{1}{4}\lambda_h(H^\dagger H)^2 + \frac{1}{2}\mu_s^2 S^2 + \frac{1}{4}\lambda_s S^4 + \frac{1}{2}\alpha S(H^\dagger H) + \frac{1}{4}\lambda_{hs} S^2(H^\dagger H) + \frac{1}{3}\beta S^3. \quad (2.3)$$

Electroweak symmetry breaking generates vacuum expectation values (vevs), v and ω , for the Higgs doublet and scalar singlet fields, respectively. The physical states are obtained by expanding around the vevs, $H \rightarrow \frac{1}{\sqrt{2}}(v+h)$ and $S \rightarrow \omega+s$, derived from the minimization conditions:

$$\left. \frac{\partial V(h, s)}{\partial h} \right|_{\substack{\langle h \rangle = v, \\ \langle s \rangle = \omega}} = 0, \quad \left. \frac{\partial V(h, s)}{\partial s} \right|_{\substack{\langle h \rangle = v, \\ \langle s \rangle = \omega}} = 0, \quad (2.4)$$

which demonstrates that the fields become coupled,

$$-\mu_h^2 + \lambda_h v^2 + \alpha\omega + \frac{1}{2}\lambda_{hs}\omega^2 = 0, \quad (2.5)$$

$$(2\mu_s^2 + \lambda_{hs}v^2)\omega + 2(\beta + \lambda_s\omega)\omega^2 + \alpha v^2 = 0. \quad (2.6)$$

These equations can generate up to eight stationary points, in addition to the typical symmetric point at the origin, $(0, 0)$. Some of these points may be degenerate, whereas others may not be physically viable. Consequently, the singlet extension in Eq. (2.3) directly influences the Higgs vacuum at the tree level, which becomes dependent on the singlet parameters after spontaneous symmetry breaking:

$$v_b = \left(\pm \sqrt{\frac{\mu_h^2 - (\alpha + \frac{1}{2}\lambda_{hs}\omega)\omega}{\lambda_h}}, \pm \sqrt{\frac{-2(\mu_s^2 + \beta\omega + \lambda_s\omega^2)\omega}{\alpha + \lambda_{hs}\omega}} \right). \quad (2.7)$$

If the singlet has a vanishing vev, $\omega = 0$, or when $|\alpha| = \frac{1}{2}\lambda_{hs}\omega$, the broken minima in Eq. (2.7) will converge to the electroweak vev, $v_{\text{EW}} \approx 246$ GeV, which is also evident from Eq.(2.5). Moreover, Eq. (2.5) indicates that at high temperatures, where the vevs become temperature-dependent, a large negative value for the cubic term, $|\alpha| > \frac{1}{2}\lambda_{hs}\omega$, can drive the electroweak phase transition towards the first-order type solely through the tree-level (TL) contribution by improving the sphaleron condition. This is a consequence of a decrease in μ_h^2 , and can significantly reduce the critical temperature as $T_c \propto \mu_h$ as will be demonstrated subsequently. This phenomenon may not be immediately apparent from Eq. (2.7) as a reduction in μ_h^2 may decrease v_b , and consequently may diminish the first-order electroweak phase transition condition, $\frac{v_c}{T_c}$, in totality. However, this is not the case, as will be demonstrated. Consequently, this extensive parameter space facilitates the

	$m_i(v, \omega)$	n_i	f_i
W^\pm	$\frac{1}{2}g_1 v$	6	$\frac{5}{6}$
Z	$\frac{1}{2}\sqrt{g_1^2 + g_2^2} v$	3	$\frac{5}{6}$
t	$\frac{1}{\sqrt{2}}y_t v$	-12	$\frac{3}{2}$
H	$m_1(v, \omega)$	1	$\frac{3}{2}$
S	$m_2(v, \omega)$	1	$\frac{3}{2}$

Table 1. Properties of the particles participating in the Coleman-Weinberg potential.

possibility of obtaining a FOEWPT. Conversely, the tree-level corrections would reduce the mixing angle and the di-Higgs boson decays for some parameter space points, potentially necessitating higher luminosity to examine the \mathbb{Z}_2 -asymmetric scenario compared with the \mathbb{Z}_2 -symmetric one [26, 34]. In addition to tree-level corrections, NLO corrections, both at zero temperature from the Coleman-Weinberg one-particle irreducible (1PI) contribution, and at finite temperature, could further catalyze the phase transition towards a FOEWPT. The Coleman-Weinberg correction to the tree-level potential is given by

$$V_{CW}^{(1)}(v, \omega) = \sum_i \frac{n_i}{64\pi^2} m_i^4(v, \omega) \left[\log \frac{m_i^2(v, \omega)}{\Lambda^2} - f_i \right], \quad (2.8)$$

where n_i corresponds to the number of degrees of freedom of particle i , f_i represents the residual fraction from dimensional regularization in the $\overline{\text{MS}}$ -renormalization scheme and Λ is the renormalization scale. The values of the corresponding parameters for each particle contributing to the Coleman-Weinberg potential are listed in Table 1. Generally, all massive particles contribute to this correction; however, owing to the large mass hierarchy among the SM particles, considering only the heavy particles (W^\pm , Z , t) provides a reasonable approximation. Because these particles are not directly coupled to the real singlet, their masses retain their SM values. Nevertheless, the expression for the Higgs boson mass differs from that of SM because of its coupling with the real singlet field. The new Higgs boson mass, in conjunction with the singlet mass, is obtained through the diagonalization of the mass matrix:

$$M = \begin{pmatrix} \frac{\partial^2 V(h, s)}{\partial h^2} & \frac{\partial^2 V(h, s)}{\partial h \partial s} \\ \frac{\partial^2 V(h, s)}{\partial h \partial s} & \frac{\partial^2 V(h, s)}{\partial s^2} \end{pmatrix}, \quad (2.9)$$

which returns,

$$m_{1,2}^2(v, \omega) = \frac{1}{4} \left[2(\mu_s^2 - \mu_h^2) + 2(\alpha + 2\beta)\omega + (\lambda_{hs} + 6\lambda_h)v^2 + (\lambda_{hs} + 6\lambda_s)\omega^2 \mp \left\{ \left[2(\mu_s^2 + \mu_h^2) - 2(\alpha - 2\beta)\omega + (\lambda_{hs} - 6\lambda_h)v^2 - (\lambda_{hs} - 6\lambda_s)\omega^2 \right]^2 + 16(\alpha + 2\beta)v^2 \right\}^{\frac{1}{2}} \right], \quad (2.10)$$

The new scalar mass is considered to be the heavier one, $m_2^2(v, \omega)$, to maintain consistency with the SM Higgs boson mass $m_h^2(v) = 2\lambda_h v^2$, which is only satisfied by $m_1^2(v, \omega)$ when all the real singlet parameters vanish. Furthermore, this analysis focuses on the kinematical region where $m_s > m_h$, necessitating that the heavier mass $m_2^2(v, \omega)$ be the new scalar mass.

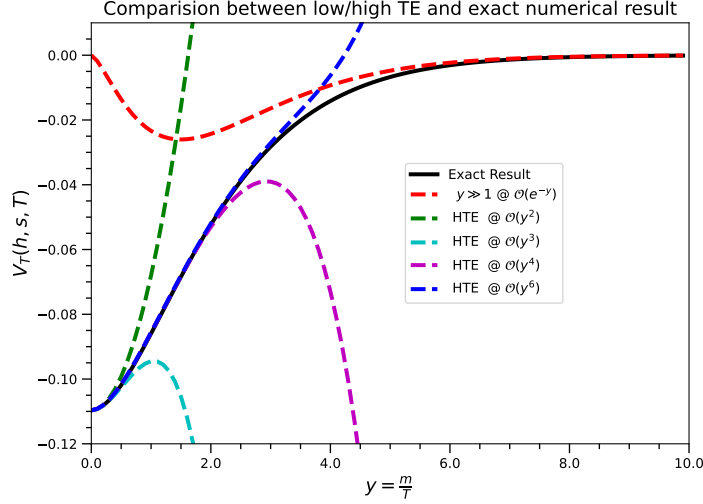


Figure 1. The dashed red curve shows the low-temperature expansion of the $V_T(y, T)$ in Eq. (2.11). By definition, it will only converge to the exact numerical calculation (solid black curve) when $m > T$ and will both coincide at $y \geq 5$. The other colored dashed curves represent the HTE of $V_T(y, T)$ at different order of expansion in y .

The finite-temperature corrections are obtained from (refer to, e.g. [3, 4, 39] for a comprehensive review),

$$V_T(y, T) = \sum_i \frac{n_i T^4}{2\pi^2} \int_0^\infty dx x^2 \log \left[1 \mp e^{-\sqrt{x^2 + y^2}} \right], \quad (2.11)$$

where, $x = \frac{p}{T}$, $y = \frac{m}{T}$, and the sign depends on the particle type (negative for bosons and positive for fermions). For non-vanishing particle masses, $y \neq 0$, the integral must be evaluated numerically. Nevertheless, a high-temperature expansion (HTE) to order $\mathcal{O}(y^6)$,

$$V_{T,B}^{\text{HTE}}(v, \omega, T) = -\frac{\pi^2 T^4}{90} + \sum_{\substack{i=Z, W^\pm, \\ H, S}} n_i \left(\frac{m_i^2 T^2}{24} - \frac{m_i^3 T}{12\pi} - \frac{m_i^4}{2(4\pi)^2} \left[\ln \left(\frac{m_i e^{-\gamma_E}}{4\pi T} \right) - \frac{3}{4} \right] \right. \\ \left. + \frac{m_i^6 \xi(3)}{3(4\pi)^4 T^2} + \mathcal{O}(m^8) \right), \quad (2.12)$$

$$V_{T,t}^{\text{HTE}}(v, \omega, T) = -\frac{21\pi^2 T^4}{180} + \frac{m_t^2 T^2}{4} + \frac{6m_t^4}{(4\pi)^2} \left[\ln \left(\frac{m_t e^{-\gamma_E}}{4\pi T} \right) - \frac{3}{4} \right] \\ - \frac{28m_t^6 \xi(3)}{(4\pi)^4 T^2} + \mathcal{O}(m^8) \quad (2.13)$$

could be a valid approximation up to $m \lesssim 3T$ as explained in Ref. [39] (See Fig. 1). In this study, we set $m_s \in [200 : 1000]$ GeV, indicating that certain scalar mass values do not conform to this approximation. However, for these values, the thermal corrections can be disregarded because in this case, $m_s > 3T$, and the low-temperature expansion will be a valid approximation, superseding the HTE, which is exponentially suppressed. Consequently, this contribution can be disregarded for this pedagogical analysis, particularly given that in \mathbb{Z}_2 -asymmetric xSM, the FOEWPT is predominantly driven by the tree-level odd terms. Therefore, the calculations can be modified according to the valid mass as follows:

- For $m_s \lesssim 3T$, which represents the majority of valid conservative parameter space points (see Fig. 2), the thermal corrections can be approximated by the HTE, such that the overall effective potential becomes,

$$V_{\text{eff}}(v, \omega, T) = V_{TL}(v, \omega) + V_T^{\text{HTE}}(v, \omega), \quad (2.14)$$

where, $V_T^{\text{HTE}}(v, \omega)$ is the sum of Eq. (2.12) and Eq. (2.13) for all bosonic and fermionic contributions, including the real scalar singlet.

- For $m_s > 3T$, which represents the majority of liberal parameter space points, the overall effective potential becomes,

$$V_{\text{eff}}(v, \omega, T) = V_{TL}(v, \omega) + \bar{V}_T^{\text{HTE}}(v, \omega), \quad (2.15)$$

where, $\bar{V}_T^{\text{HTE}}(v, \omega)$ is given by the sum of Eq. (2.12) and Eq. (2.13) but with the scalar singlet contribution excluded from Eq. (2.12), retaining only the contributions of h , Z , W^\pm particles.

Notably, the fractional term proportional to m_i^4 in Eq. (2.12), and m_t^4 in Eq. (2.13), cancels out with the corresponding CW correction in Eq. (2.8), whereas the logarithmic part is reduced to $\log\left[\frac{e^{2\gamma_E} T^2}{\Lambda^2}\right]$, where $\frac{e^{2\gamma_E} T^2}{\Lambda^2} \approx \mathcal{O}(1)$, if the scale is considered equal to the temperature. For other scales, one can qualitatively estimate the relative weight of the CW corrections by examining the possible shift in the Higgs vacuum structure when considering CW contributions as

$$V_{\text{eff}}(v, \omega) = V_{TL}(v, \omega) + V_{CW}^{(1)}(v, \omega). \quad (2.16)$$

Then,

$$\frac{1}{v} \nabla(\Delta V_{\text{eff}}(v, \omega)) = \frac{1}{v} \frac{\partial V_{CW}^{(1)}}{\partial v} \quad (2.17)$$

$$= \sum_i \frac{n_i \rho_i}{32\pi^2} \left[\log\left(\frac{m_i^4}{\Lambda^4}\right) - 2f_i + 1 \right] v^2, \quad (2.18)$$

where $m_i = \rho_i v$, and ρ_i is the coefficient of v for each particle i in Table 1. The logarithmic term in Eq. (2.18) is attenuated by the corresponding contributions from the thermal

corrections and the running of the couplings, which also partially cancel the CW corrections. Hence it can be disregarded in comparison to the other terms in brackets,

$$\frac{1}{v} \frac{\partial V_{CW}^{(1)}}{\partial v} \approx \sum_i \frac{n_i \rho_i}{32\pi^2} [1 - 2f_i] v^2, \quad (2.19)$$

This results in an increase in the coefficients of v^2 in Eq. (2.5) and Eq. (2.6), which is smaller than 0.005 when only including the effect of t , Z , W^\pm . This becomes even smaller when the effects of H, S are added because they have an overall negative value for the bracket in Eq. (2.19). Consequently, this correction can maximally change Higgs vev by a factor smaller than 1% when compared to the leading v^2 -coefficients; $\lambda_h \approx 0.13$ and α which could be even larger than λ_h for non-vanishing ω , when $|\alpha| > \frac{1}{2} \lambda_{hs} \omega$. Therefore, for an approximate understanding of the thermal evolution of Higgs vev, one can disregard the CW correction to the effective potential as well.

In addition to thermal corrections, the contributions from the rings diagrams must be considered to secure the cubic mass term¹ in Eq. (2.12) from having imaginary values for m_1, m_2 at certain values of the vevs [17], indicating the breakdown of perturbative expansion at high temperatures due to the quartic coupling running with temperature [40, 42, 43]. This issue can be resolved by incorporating higher-order IR-divergent contributions, ring (Daisy) diagrams, which, according to Ref. [17] takes the following form:

$$V_{\text{rings}} = -\frac{T}{12\pi} \left[\left(m^2(v, \omega) + \frac{\lambda}{4} T^2 \right)^{\frac{3}{2}} - m^3(v, \omega) \right]. \quad (2.20)$$

This corresponds to the shift $m_{1,2}^3 \rightarrow M_{1,2}^3 = \left(m_{1,2}^2(v, \omega) + \frac{\lambda}{4} T^2 \right)^{\frac{3}{2}}$, where the gauge bosons do not lead to any imaginary parts. Therefore, at very high temperatures, $\lambda T^2 \gg m_{1,2}^2$, the scalar cubic term is reduced to a pure temperature term, independent of the fields. This implies that the cubic term coefficient will be exclusive to the vector gauge boson contributions in this approximation, and will not receive any further corrections in xSM. Considering the main corrections in Eq. (2.11) and Eq. (2.20), the effective potential becomes,

$$\begin{aligned} V_{\text{eff}}(v, \omega, T) &= V_{TL}(v, \omega) + V_T^{\text{HTE}}(v, \omega) + V_{\text{rings}} \\ &= \frac{1}{2} C(T^2 - T_0^2) v^2 - E T v^3 + \frac{1}{2} \alpha v^2 \omega + \frac{1}{4} \lambda_{hs} v^2 \omega^2 \\ &\quad + \frac{1}{4} \lambda_h v^4 + \frac{1}{2} D(T^2 - T_1^2) \omega^2 + \frac{1}{3} \beta \omega^3 + \frac{1}{4} \lambda_s \omega^4 + \mathcal{O}\left(\frac{1}{T^2}\right), \end{aligned} \quad (2.21)$$

¹This term characterizes the bosonic contributions, as it only originates from the vanishing Matsubara mode, see [40, 41], but the gauge boson terms will not generate any imaginary output for all values of v , as their mass can never be negative.

where,

$$C = \frac{1}{4} \left(\frac{1}{4} (3g_1^2 + g_2^2) + 2y_t^2 + \lambda_h + \frac{\lambda_{hs}}{6} \right), \quad (2.22)$$

$$E = \frac{1}{32\pi} (2g_1^2 + (g_1^2 + g_2^2))^{\frac{3}{2}}, \quad (2.23)$$

$$D = \frac{1}{4} \left(\lambda_s + \frac{\lambda_{hs}}{6} \right), \quad T_0^2 = \frac{\mu_h^2}{C}, \quad T_1^2 = \frac{-\mu_s^2}{D}, \quad (2.24)$$

and $\mathcal{O}(\frac{1}{T^2})$ represents corrections arising from the m^6 -term in the HTE. The vevs then become temperature dependent,

$$v_b(T) = \left\{ \frac{6ET \pm \sqrt{36E^2T^2 - 8\lambda_h[2C(T^2 - T_0^2) + (2\alpha + \lambda_{hs}\omega)\omega]}}{4\lambda_h}, \right. \\ \left. \pm \sqrt{\frac{-2[D(T^2 - T_1^2) + \beta\omega + \lambda_s\omega^2]\omega}{\alpha + \lambda_{hs}\omega}} \right\}. \quad (2.25)$$

The above equation represents the temperature-dependent version of Eq. (2.7), and it can be rewritten using the relations in Eq. (2.24) as,

$$\frac{v_b(T)}{T} = \frac{3E}{2\lambda_h} + \sqrt{\frac{\mu_h^2}{T^2} + \frac{9E^2}{4\lambda_h^2} - \frac{C}{\lambda_h} - \xi(T)}, \quad (2.26)$$

where $\xi(T) = \frac{(2\alpha + \lambda_{hs}\omega)\omega}{2\lambda_h T^2}$. At the critical temperature in the SM, the sphaleron condition in Eq. 2.26 returns $\frac{v_c}{T_c} = \frac{2E}{\lambda_h} \approx 0.15$, where $T_c^{\text{SM}} = \frac{\mu_h}{\sqrt{C(1 - \frac{2E^2}{\lambda_h C})}}$ and $\xi(T) = 0$. This means

that the sphaleron condition in the xSM is primarily improved by the $\xi(T)$ -correction term, which can contribute significant negative values to Eq. 2.26 for large negative values of the odd \mathbb{Z}_2 -asymmetric term $\alpha H^\dagger H S$. An additional supporting correction arises from the decrease in the critical temperature due to the λ_{hs} portal coupling correction to the C -term, as per Eq. (2.22) and the correction to the μ_h^2 term given in Eq. (2.5). The critical temperature is determined from the degeneracy condition,²

$$V_{\text{eff}}(0, \omega; T_c) = V_{\text{eff}}(v_c, \omega; T_c), \quad \left. \frac{\partial V_{\text{eff}}(v, w, T_c)}{\partial v} \right|_{\langle v \rangle=0} = \left. \frac{\partial V_{\text{eff}}(v, w, T_c)}{\partial v} \right|_{\langle v \rangle=v_c}, \quad (2.27)$$

which yields,

$$T_c^{\text{xSM}} \approx 6.6 \times 10^{-3} \left(\frac{\mu_h}{\sqrt{C}} \right)^{\text{xSM}} \left[1 - \frac{(\alpha + \frac{1}{2}\lambda_{hs}\omega)\omega}{\mu_h^2} \right]^{\frac{1}{2}} T_c^{\text{SM}}. \quad (2.28)$$

²We only consider a one-step phase transition, assuming that the scalar singlet field evolved a non-vanishing vev, which remains the same at T_c . In principle, a two-step phase transition mainly accounts for a shift in the effective potential that can affect the gravitational-wave spectrum, while barely affecting the value of the critical temperature [31].

Where $\left(\frac{\sqrt{C}}{\mu_h}\right)^{SM} \approx 6.6 \times 10^{-3}$. For large negative values for α , $|\alpha| > \frac{1}{2}\lambda_{hs}\omega$, the square bracket in Eq. (2.28) becomes greater than one; however μ_h simultaneously decreases and the C -term increases, which collectively leads to a significant decrease in the critical temperature in xSM, $T_c^{\text{xSM}} < T_c^{\text{SM}}$.

This approximate analytical investigation of the xSM extension is corroborated by the numerical methods employed to account for the full NLO (CW and finite temperature) corrections to the tree-level potential at different renormalization scales (conservative and liberal categories, see later) in order to address the theoretical uncertainties in the FOEWPT parameter space points, which are necessary for accurately exploring the muon collider. As illustrated in Fig. 2, the improvement of the sphaleron condition by the xSM extension is evident, as is the decrease in critical temperature due to the singlet contribution to the C and μ_h^2 -terms, as demonstrated in Fig. 3 for various singlet mass values.

2.1 First-Order Electroweak Phase Transition Parameter Space within the xSM

Catalyzing a FOEWPT through the real singlet extension depends on the parameter space points, particularly on the \mathbb{Z}_2 -asymmetric parameters and the Higgs-scalar quartic coupling, as shown in Eqs. (2.26). The additional scalar degree of freedom introduces five free parameter $\{\mu_s^2, \lambda_s, \alpha, \beta, \lambda_{hs}\}$ which need to be determined. In [22, 31, 38, 44], a set of diverse constraints, stemming from theoretical and phenomenological sources, were discussed to restrict these parameters,

- The stability of the effective potential necessitates positive dimensionless quartic couplings, $(\lambda_h, \lambda_s, \lambda_{hs}) > 0$.
- The validity of perturbative expansion requires quartic couplings to be smaller than unity, $(\lambda_s, \lambda_{hs}) \in [0 : 4\pi]$.
- Electroweak symmetry breaking necessitates a positive determinant of the mass matrix in Eq. (2.9) as $(v_{\text{EW}}, \omega_{\text{EW}})$ should constitute the true global minimum, which requires, $4\lambda_h\lambda_s - \lambda_{hs} > 0$.
- The electroweak precision observables (EWPO) were included, where the scalar decay into gauge boson pairs modifies the S, T, ρ, U parameters.
- Higgs boson branching ratio corrections owing to mixing with the scalar, in addition to the absence of exotic Higgs boson decays, were applied. This shifts the scalar mass towards higher values and constrains the (μ_s, α, β) parameters.

We used the values obtained in Ref. [45], in which nearly identical constraints were applied with minor variations. In this study, valid points satisfying the sphaleron condition $\frac{v_c}{T_c} > 1$ were obtained through a scan using the **PhaseTracer** package [46], which tracks vacuum evolution by evaluating the thermal integral of Eq. (2.11) numerically by employing the methods described in [47, 48], rather than the HTE approximation discussed in the previous calculations to obtain an approximate understanding of xSM. Furthermore, the ranges

Parameter	Range
μ_s	$[-2000, 2000]$ GeV
λ_s	$[10^{-4}, 1.5]$
λ_{hs}	$[0, 5]$
α	$[-1000, 0]$ GeV
β	$[-1800, 1800]$ GeV

Table 2. Ranges of xSM parameters obtained from theoretical and phenomenological constraints used in Ref. [45].

of the “portal” coupling λ_{hs} , and singlet quartic coupling λ_s , were set to be quite loose in [45], as listed in Table 2. The rationale behind this approach is that for colliders to exclude the possibility of a strong FOEWPT (SFOEWPT), the candidate parameter space points should be relatively broad.

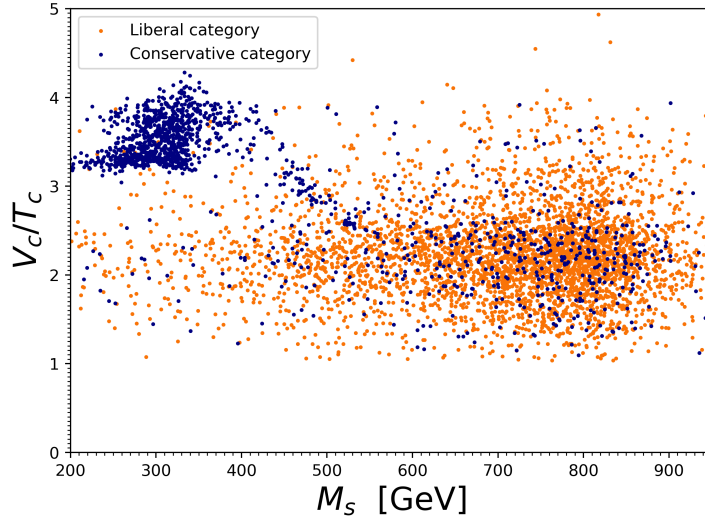


Figure 2. Verification of the sphaleron condition against the singlet scalar mass range, as obtained from the xSM parameters.

The values of the λ_{hs} coupling control the shift in the quadratic correction on C from the SM expectation, and consequently improve the sphaleron condition. However, this raises concerns regarding the validity of the perturbative expansion and its sensitivity to theoretical uncertainties related to the scale and gauge dependencies of the thermal parameters. This consideration is crucial not only for analyzing specific points, but also for comprehending the parameter space [49, 50]. According to [45], the dominant uncertainty originates from the slow convergence of perturbation theory which is manifested in the dependence on an arbitrary renormalization scale. We follow Ref. [45] and define a

“conservative” point as a point that admits an SFOEWPT for a group of eight scale and gauge variations, with at least one of these variations possessing a Higgs field vev within 246 ± 30 GeV, that also corresponds to a transition to the absolute (i.e. deepest) minimum of the potential. On the other hand a “liberal” point satisfies SFOEWPT for one of the eight scale and gauge variations and the Higgs vev condition for any other. See Ref. [45] for further details.

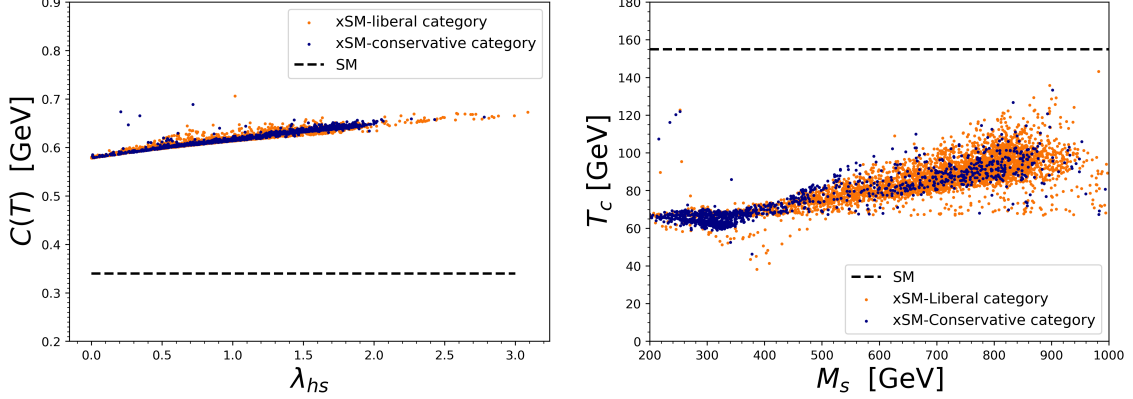


Figure 3. The left panel shows the correction to the quadratic thermal term from the λ_{hs} , while the right panel shows the drop in the critical temperature obtained from the xSM. The observed decrease in the critical temperature and increase in the $C(T)$ term collectively enhance the sphaleron condition.

A substantial number of parameter space points fulfill the SFOEWPT sphaleron condition out of the $\mathcal{O}(10^6)$ points generated according to Table 2. The SFOEWPT condition is plotted against the scalar mass in Fig. 2 for *conservative* and *liberal* categories. The observation that *conservative* category values shift more towards lower values of scalar mass, unlike *liberal* values, is a good indicator that this category can be verified by current collider searches. For instance, the LHC searches for an SM-like Higgs boson [51], which may lead to the exclusion of the conservative category.

The portal coupling λ_{hs} improves the SFOEWPT condition primarily through the correction it contributes to in the quadratic C term, which subsequently reduces the critical temperature. This phenomenon is illustrated in Fig. 3 (left panel) which demonstrates the increase in the C -term with λ_{hs} , contrary to the SM expectation. The right panel of Fig. 3 shows the tendency toward a lower critical temperature compared to the SM expectation, for both the Conservative and Liberal categories. Furthermore, the valid parameter points exhibit a propensity to concentrate towards lower values of the quartic couplings (λ_s, λ_{hs}), as shown in Fig. 4, which indicates favorable behavior regarding the validity of perturbative expansion.

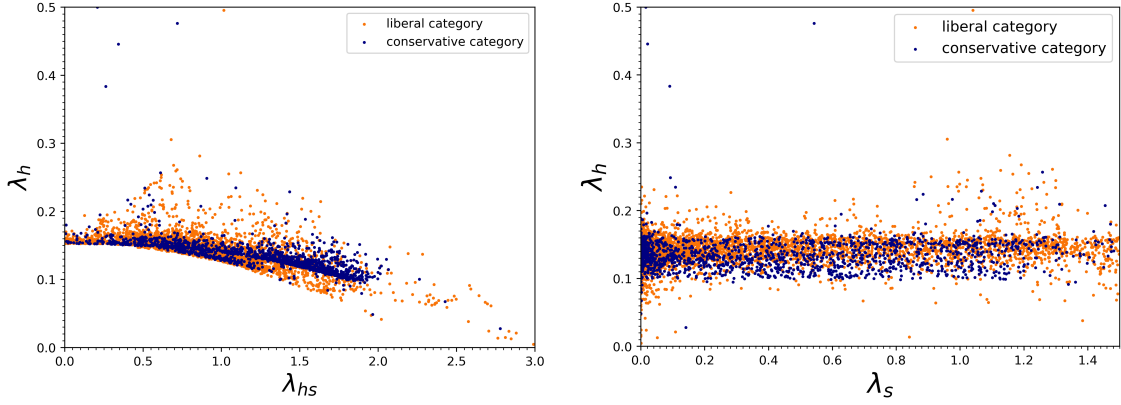


Figure 4. The dimensionless quartic couplings are shifted more towards lower values, which is a preferred behaviour, as required by the validity of the perturbative expansion.

3 The Electroweak Phase Transition at Colliders

A direct test for SFOEWPT could be derived from the gravitational waves emanating from bubble dynamics. Specifically, sound waves in the plasma and magneto-hydrodynamic turbulence generate gravitational waves that are expected to peak at low frequencies ranging from mHz to 10 Hz. Collider searches provide another promising and complementary approach for verifying the nature of EWPT. This is attributable to the fact that the catalyst of the FOEWPT, the singlet scalar field in this instance, can be probed either directly through resonant production of a new scalar, if its mass is within the range of current and future searches, or indirectly, through precise measurements of potential deviations in the Higgs boson couplings from the SM expectation. In contrast to gravitational wave detection, which can only be produced from FOEWPT, collider searches can be sensitive to SFOEWPT as well; however, this is more challenging owing to the weak mixing with the Standard Model particles.

3.1 Direct Singlet Production at Colliders

The mass of the new scalar particle in xSM is expected to be of $\mathcal{O}(T_{\text{EW}})$, which suggests the possibility of resonant production at colliders [26]. At zero temperature, i.e. in the collider scenario, the mass of the singlet-like scalar is given by $m_2(v_{\text{EW}}, \omega_{\text{EW}})$, Eq. (2.10), which yields a scalar mass in the range $m_s \in [200, 1000]$ GeV, when utilizing the range of parameters as shown in Fig. 2. This can be approximated using the curvature of the effective potential in Eq. (2.21),

$$\begin{aligned}
 m_s^2(0) &= \frac{\partial^2 V_{\text{eff}}}{\partial s^2} \\
 &= \frac{1}{2} \lambda_{hs} v_{\text{EW}}^2 - D(T_1^2) + 2\beta \omega_{\text{EW}} + 3\lambda_s \omega_{\text{EW}}^2 \\
 &= \frac{\lambda_{hs}}{6} \left(3v_{\text{EW}}^2 - \frac{6}{\lambda_{hs}} (DT_1^2 - 2\beta\omega - 3\lambda_s \omega^2) \right), \tag{3.1}
 \end{aligned}$$

This coincides with the results of [26], if we set $T_{\text{EW}}^2 = \frac{6}{\lambda_{hs}}(DT_1^2 - 2\beta\omega - 3\lambda_s\omega^2)$. This mass range is within the scope of prospective future collider experiments such as a muon collider, where a new scalar can be produced resonantly through one of the main production channels $\mu^+\mu^- \rightarrow s \rightarrow XX$. The probability of direct detection is more promising for channels with charged fermions in the final states (i.e. four leptons, $l^-l^+l^-l^+$, or four quarks, $b\bar{b}b\bar{b}$), where the invariant mass can be fully reconstructed.

Due to the anticipated low mass of the new scalar, $\lesssim \mathcal{O}(\text{TeV})$, both hadron and lepton colliders are valid options for detection. Previous studies [26, 27] have confirmed that a 100 TeV proton-proton collider can substantially explore this parameter space. Recently, there has been a growing interest in muon colliders, which can explore the same parameter space efficiently, at a significantly lower center of mass energy ($\sqrt{s} \in [3 - 10] \text{ TeV}$) [26, 36]. In a muon collider, most of the available energy is consumed in the hard process, which directly relates the resonance peak to the center of mass energy according to $\frac{\sqrt{s}}{2m_s} \approx 1.7$ as demonstrated in ref. [26]. This characteristic is unique for lepton colliders, unlike hadron colliders where E_{CM} of the beam differs from that of the parton beams, necessitating integration over the parton density functions. Furthermore, a muon collider will not suffer from the huge QCD radiation resulting from the initial state as in the case of hadron colliders, nor will its energy be dissipated in the large synchrotron radiation as in an electron collider. Notably, the optimal channel for the single production of a new scalar is through vector boson fusion (VBF), mainly W^+W^- fusion, which contributes $\sim 90\%$ of the total cross section [36, 37].

3.2 Indirect Evidence: Modification of Higgs Boson Couplings

The most significant terms for indirect detection in the extended potential are those that couple the new scalar to the Higgs field,

$$V(h, s) \supset \frac{1}{2}\mu_m SH^\dagger H + \frac{1}{4}\lambda_m S^2 (H^\dagger H)^2, \quad (3.2)$$

which consequently form a “portal” of the new scalar to the other SM particles. The other self-interaction couplings of the new scalar do play a crucial role in determining the points of EWPT but do not substantially affect phenomenological studies.³ The terms in Eq. (3.2) inevitably lead to mixing between H and S and consequently the new scalar “inherits” interactions with SM particles. The mass eigenstates are obtained using the rotation angle θ , after symmetry breaking as follows:

$$\begin{pmatrix} h_1 \\ h_2 \end{pmatrix} = \begin{pmatrix} \cos \theta & \sin \theta \\ -\sin \theta & \cos \theta \end{pmatrix} \begin{pmatrix} h \\ s \end{pmatrix}, \quad (3.3)$$

where the mixing angle is given by,

$$\cot \theta = \frac{2M_{hs}^2}{M_{hh}^2 - M_{ss}^2 + \sqrt{(M_{hh}^2 - M_{ss}^2)^2 + 4M_{hs}^4}}, \quad (3.4)$$

³For example, the λ_s coupling only appears in the daisy resummation part of the effective potential [34].

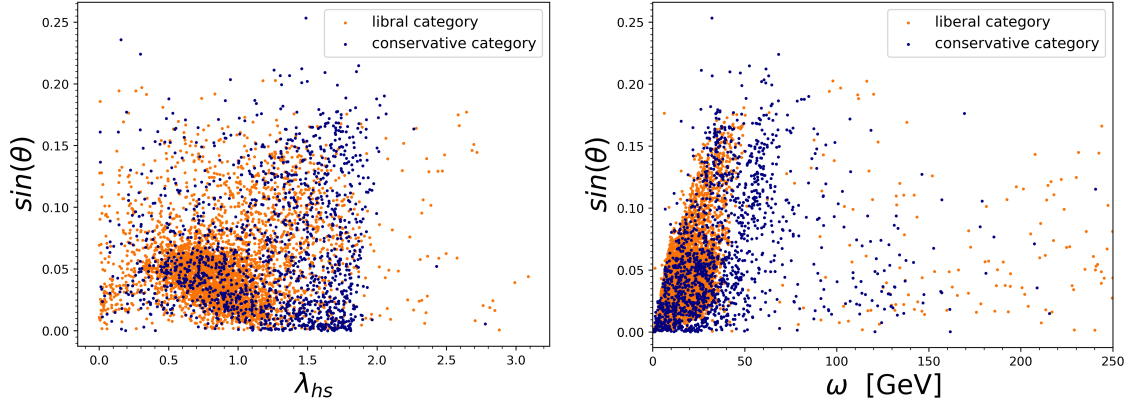


Figure 5. The Higgs-singlet mixing angle against the portal coupling λ_{hs} and singlet vacuum expectation value, ω .

where M_{hh}^2 , M_{ss}^2 , M_{hs}^2 are the components of the mass matrix in Eq. (2.9). Consequently, the SM-like Higgs boson couplings must be adjusted according to:

$$g_{hXX}^{\text{SM}} \rightarrow g_{h_1XX}^{\text{SM}} \cos \theta - g_{h_2XX}^{\text{SM}} \sin \theta. \quad (3.5)$$

Here, $g_{h_1XX}^{\text{SM}} \cos \theta$ represents the scaling of the original Higgs boson couplings, and $g_{h_2XX}^{\text{SM}} \sin \theta$ represents the new scalar couplings to the XX -SM-particles. This opens up a range of possible precision tests such as small deviations in SM-like Higgs boson production rates according to $\sigma_h^{\text{BSM}} = \cos^2 \theta \times \sigma_{h_1}^{\text{SM}}$. Another significant phenomenological test would be the deviation of Higgs boson trilinear self-coupling from the SM expectation, where after symmetry breaking this term becomes,

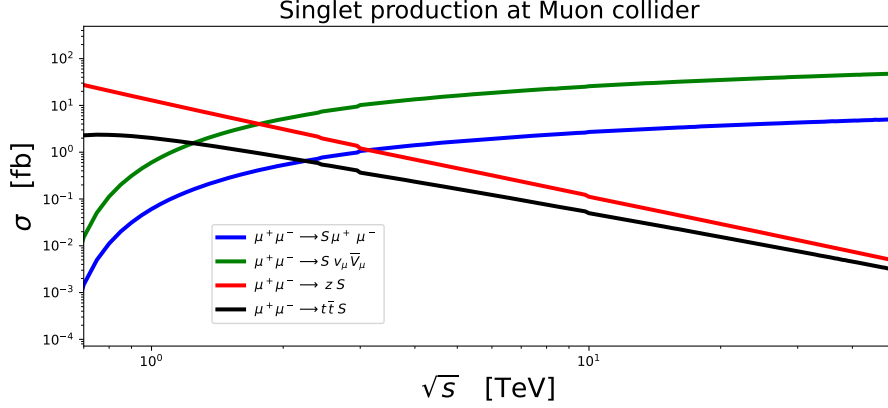
$$\lambda_{hhh} = \frac{1}{4} \left[c_\theta (\lambda_h c_\theta^2 + \lambda_{hs} s_\theta^2) v_{\text{EW}} + (\alpha + \lambda_{hs} \omega) c_\theta^2 s_\theta + \frac{4}{3} (\beta + 3\lambda_s \omega) s_\theta^3 \right], \quad (3.6)$$

where $c_\theta = \cos \theta$ and $s_\theta = \sin \theta$. In [34], a scan was performed over the possible parameter space which led to FOEWPT demonstrating a significant difference between $\lambda_{hhh}^{\text{BSM}}$ and $\lambda_{hhh}^{\text{SM}}$, that could be as big as $\frac{\lambda_{hhh}^{\text{BSM}}}{\lambda_{hhh}^{\text{SM}}} \sim 1.3$. Conversely, the current precision of the Higgs boson couplings and branching ratios favor a small value of the mixing angle, which in our study was adopted to better constrain the parameter space using the additional phenomenological constraint in Eq. (3.4). This constraint indicates that the points that satisfy SFOEWPT favor smaller values of λ_{hs} and singlet vev, ω , as depicted in Fig. 5, which is in agreement with the perturbativity constraint. In this study we are focusing on the possible direct detection at a muon collider and save the possible precision tests of the Higgs couplings at muon collider for future work.

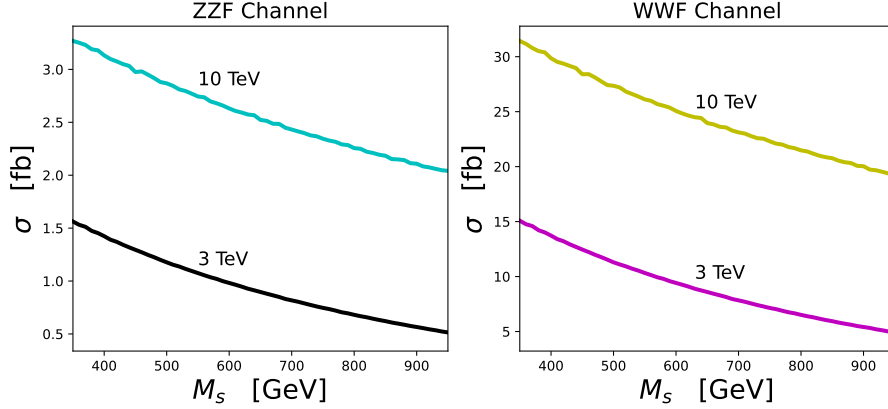
4 Constraints on the xSM at a Muon Collider

The dominant production mechanism of the new scalar (S) at a muon collider is vector boson fusion (VBF), with W^+W^- fusion (WWF) dominating ZZ fusion (ZZF) as reported

in previous studies [36, 37, 52, 53]. In our analysis, we set the muon beam center of mass



(A)



(B)

Figure 6. The different production mechanisms are illustrated in (A), which also shows that VBF is dominated by W^+W^- fusion (WWF) (green curve), which is further confirmed in (B), showing that WWF accounts nearly for 90% of VBF. (B) also shows that the S -production cross section is only marginally sensitive on its mass M_S . The plots have been generated through `MadGraph5_aMC@NLO` simulations at parton level for $\sin\theta = 1$.

energy to $\sqrt{s} = 3$ TeV, where VBF became the main production channel, as illustrated in Fig. 6. The mass range of the scalar was taken to be $M_S \in [250 : 1000]$ GeV, stemming from the thermal correction constraint as discussed in the previous section. Consequently, the S decay into two SM-like Higgs bosons becomes possible given a non-vanishing α . Based on the potential in Eq. (2.3), the new scalar will then primarily decay either directly into two Higgs bosons (h_1h_1), or into two vector bosons through the mixing between the two scalars,

$$\mu^+\mu^- \rightarrow S\mu^+\mu^-(\nu_\mu\bar{\nu}_\mu) \rightarrow XX\mu^+\mu^-(\nu_\mu\bar{\nu}_\mu), \quad (XX = h_1h_1, W^+W^-, ZZ).$$

The final states obtained from these scalars encompass different topologies, which can be classified into two main categories: pure visible states such as $4l$, $4q$, $2l2q$, $2q2\gamma$, and

visible-invisible mixed states such as $l\nu 2q$, $2l2\nu_l$, $2q2\nu_l$. For each final state, we considered the backgrounds originating from all possible channels that would produce the same final state as without the resonant production of the S scalar. Therefore, the invariant mass is expected to serve as a highly effective discriminant against the substantially larger background. In our analysis, we initially filter the signal through the invariant mass computed for each specific topology, and subsequently refine the remaining events based on their transverse momentum and pseudorapidity window, obtained by direct comparison of the generated signal to the dominant background. An advantage of a muon collider, that becomes apparent in this analysis, is the ability to track the missing energy that may be present in the final states, and account for it in the invariant mass calculations, as we will see below. In the remaining parts of this section, we enumerate the channels that we have investigated and provide their corresponding expected sensitivities. Subsequently, we project these sensitivity plots onto the FOEWPT xSM parameter space, to assess the potential of the proposed muon collider to provide meaningful constraints.

4.1 Event Generation

Both signal and background Monte Carlo events were generated at the parton level using MadGraph5_aMC@NLO [54] (MG5_aMC), while the scalar decays to gauge/Higgs bosons were generated in HERWIG 7 [55–61], along with the parton showering, underlying event and hadronization. The HwSim plugin for HERWIG 7 [62] was used to generate ROOT [63] files for all event samples. Signal events were produced in MG5_aMC by using the `loop_sm_scalar` model [45].⁴ Due to background events at a muon collider occurring at much lower rates

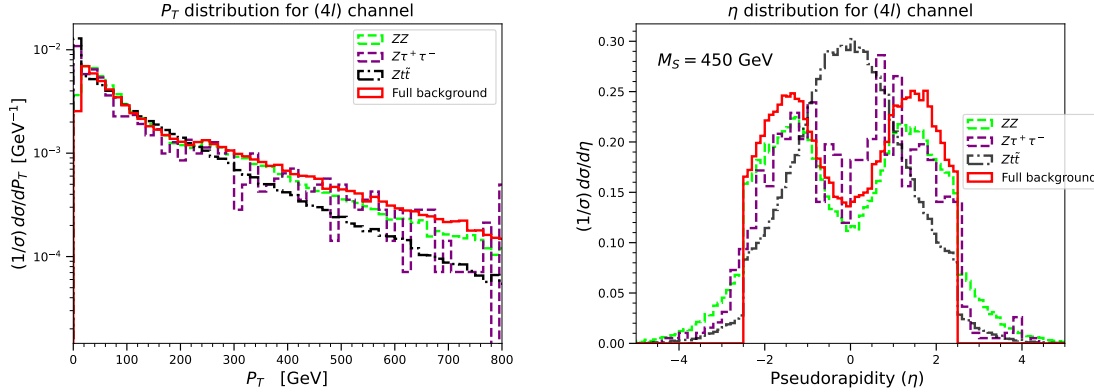


Figure 7. The summed background (red curve) is evidently the sum of all subdominant background resulting from ZZ , $Z\tau^+\tau^-$, $Zt\bar{t}$ as seen in transverse momentum distribution (left) and pseudorapidity distribution (right).

than at a hadron collider, we took into account all the possible background events for each final state by generating it directly in MG5_aMC, without importing the `loop_sm_scalar`

⁴We used electron-positron beams for event generation instead of muon-antimuon beams since HERWIG 7, at the time of writing, cannot readily handle muons in the initial state. This does not affect our analysis at all because of lepton universality, and the irrelevance of the lepton mass at high energies.

model. For example, for $\mu^+\mu^- \rightarrow \mu^+\mu^- S \rightarrow \mu^+\mu^- l^+ l^- l^-$, we generated the combined background, $\mu^+\mu^- \rightarrow \mu^+\mu^- l^+ l^- l^-$. Combined process generation implicitly contains all the dominant backgrounds resulting from ZZ , $Z\tau^+\tau^-$, $Zt\bar{t}$, \dots . We have examined this claim by comparing the kinematic distributions (P_T, η) of the $4l$ -combined background to the dominant $4l$ background sources, such as those coming from ZZ , $Z\tau^+\tau^-$, $Zt\bar{t}$, and confirmed that the combined $4l$ - background is indeed almost identical to the sum of the individual dominant backgrounds, as is evident in Fig. 7. Therefore, in our analysis, we compare the signals to the combined backgrounds, instead of just the main ones.

4.2 $4l$ Final States

The four-lepton final state originates from $S \rightarrow ZZ$, and its dominant background is $\mu^+\mu^- \rightarrow 2l^+2l^-\mu^+\mu^-$ and $\mu^+\mu^- \rightarrow 2l^+2l^-\nu_\mu\bar{\nu}_\mu$. The signal leptons are expected to have a higher transverse momentum compared to the background ones, as they originate from Z -boson decays, which suggests a constraint on the transverse momentum in terms of Z -boson mass as $\sim P_T(l^\pm) \geq \frac{2}{5}M_Z$. This assumption was verified by comparing the signal-background transverse momentum distributions for the charged leptons, which showed signal domination in the region $\sim 50 \text{ GeV} \leq P_T(l^\pm) \leq 400 \text{ GeV}$. Consequently, we identified any oppositely charged same-flavour leptons whose $P_T(l^\pm) \geq \frac{2}{5}M_Z$, and their invariant mass peaked around the Z -boson mass, $0.8M_Z \leq M(l^+l^-) \leq 1.2M_Z$ as valid pairs resulting from Z -boson decay. This works as a strong signal-background separator because the leptons produced from the background generated in `MG5_aMC@NLO` are sourced from different mediators, as discussed in the previous section. This is in contrast to the signal case where they are mainly produced from Z -bosons, $S \rightarrow ZZ$. Then, the surviving pairs were further constrained by requiring the invariant mass of the two pairs to be in the vicinity of the scalar mass, $M_s - 50 \text{ GeV} \leq M(l^+l^-l^+l^-) \leq M_s + 50 \text{ GeV}$, which further suppressed the background events, as they were not resonantly produced in this range. A sharp constraint in the invariant mass of the four leptons, $\Delta M(l^+l^-l^+l^-) = 50 \text{ GeV}$, was adopted due to the good expected resolution in the reconstruction of the charged leptons. These combined invariant mass cuts led to significant suppression of background events, with $< 10\%$ surviving, compared to signal events, where $\sim 50\%$ survived, as can be seen in Fig. 8 (C). The remaining events were further constrained using the transverse momentum and pseudorapidity of pairs of oppositely charged leptons, see Fig. 8 (A,B). The selected ranges for $P_T(l^+l^-), \eta(l^+l^-)$ are automated for each M_s value where only regions that contain $N_s \geq 3.5N_b$ for $P_T(l^+l^-)$ and $N_s \geq 4.5N_b$ for $\eta(l^+l^-)$ were selected.⁵ These ranges change according to the M_s value, as can be seen in Table 3. The efficiencies obtained via this analysis were then used to estimate the expected exclusion cross section using,

$$\mathcal{S} = \frac{S}{\sqrt{B + (\alpha B)^2}}, \quad (4.1)$$

where $S = \varepsilon_s L \sigma_s$ is the signal number of events, and $B = \varepsilon_b L \sigma_b$ is the background number of events. The exclusion limit \mathcal{S} is set to 2, corresponding to a 95% confidence level (C.L.)

⁵ N_s, N_b are the number of signal and background events respectively.

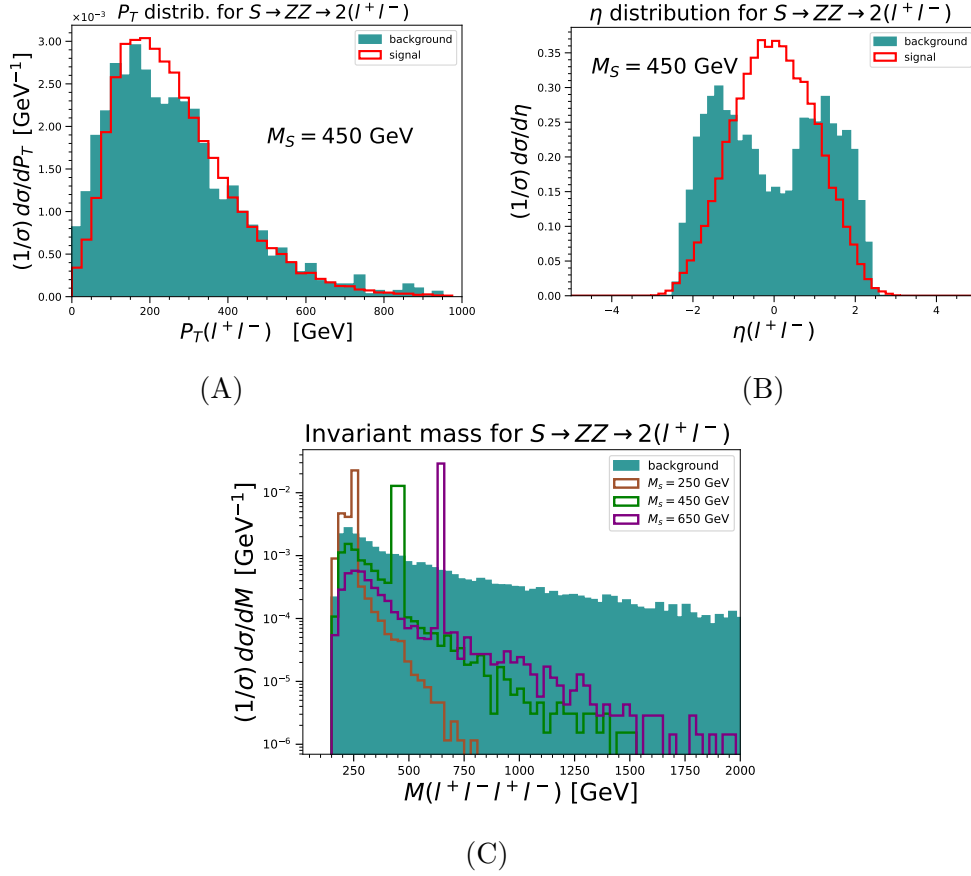


Figure 8. Transverse momentum and pseudorapidity distributions for signal events of $M_S = 450$ GeV are shown in (A) and (B) respectively. The plot in (C) shows the invariant mass distribution of the four leptons ($M(4l)$) for different values of the S masses. The backgrounds considered are the sum of all backgrounds resulting from $\mu^+\mu^- \rightarrow \mu^+\mu^- 2l^+2l^-$.

M_S [GeV]	250	500	750	1000
$P_T(l^+l^-)$ [GeV]	86 : 956	37 : 877	18 : 938	76 : 916
$ \eta(l^+l^-) $	< 1.15	< 1.35	< 1.75	< 1.75

Table 3. Samples of transverse momentum and pseudorapidity cuts for $4l$ channel, automated for different values of the scalar mass.

exclusion.

The four-lepton invariant mass cut, $M(l^+l^-l^+l^-)$, is the most crucial constraint in this analysis, as backgrounds lack resonant production, so we calculated the uncertainty in our calculations by repeating the analysis for different invariant mass ranges, $\Delta M(l^+l^-l^+l^-) = 100$ GeV where both ε_s , ε_b would deviate from the previous one leading to uncertainty in

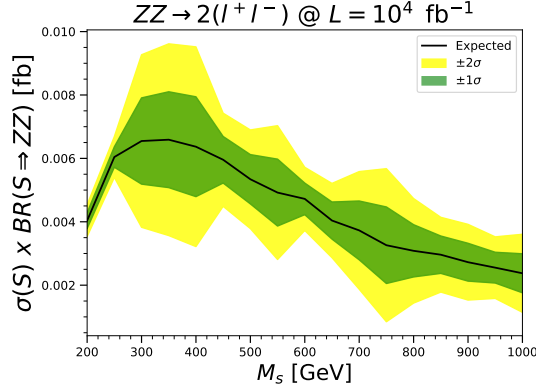


Figure 9. Cross section exclusion curve for $\sigma(S) \times \text{BR}(S \rightarrow ZZ)$ with $ZZ \rightarrow 4l$. The green and yellow intervals correspond to the 1σ and 2σ confidence levels.

the signal cross section given by,

$$U(\sigma_s) = \frac{\sigma_s(\varepsilon_s, \varepsilon_b)}{2} \sqrt{\left(\frac{\delta\varepsilon_s}{\varepsilon_s}\right)^2 + \left(\frac{\delta\varepsilon_b}{\varepsilon_b}\right)^2}. \quad (4.2)$$

Finally, the resulting sensitivity plot for a luminosity of 10^4 fb^{-1} is shown in Fig. 9, at 68% and 95% C.L.

4.3 $4q$ Final States

The $4q$ final state can result from three different pathways: $S \rightarrow ZZ, W^+W^-, hh$, and could also provide strong constraints. The main background is similar to those discussed in the previous channel, with $l \rightarrow q$. In principle, the jets originating from (ZZ, W^+W^-, hh) decays will have almost identical kinematics due to the approximate symmetry in the Z, W^\pm, h masses especially for $M_S \gg M_Z, M_{W^\pm}, M_h$. Nevertheless, the differences in the branching ratios of Higgs boson and weak gauge boson decays into quarks will lead to a deviation in the kinematical behavior of the two cases, especially for the transverse momentum and invariant mass distributions, as can be seen in Fig. 10 (A,C). These differences can be further investigated by tracking the jet's origin, and this can play a vital role in exploring the \mathbb{Z}_2 nature of xSM. Hence, this specific channel, which has not been explored sufficiently to date, to the best of our knowledge, can further constrain the parameter space of FOEWPT. This proves to be an additional advantage of a muon collider, in which such a channel could be explored with much less effort than at hadron colliders due to the lower QCD backgrounds. A detailed study of these differences is left for future work. Jets were clustered using **FastJet** (v3.3.2) [64], where the anti-kT algorithm [65–67] with a radius parameter $R = 0.4$ was chosen to be the default jet clustering algorithm. The calculation of the invariant mass for this channel is more challenging than in the previous one, mainly due to the high tendency of quarks to radiate via QCD. This means that we cannot simply calculate the invariant mass as previously using $M^2(4j) = \left(\sum_{i=1}^4 p(J_i)\right)^2$. Instead, for each

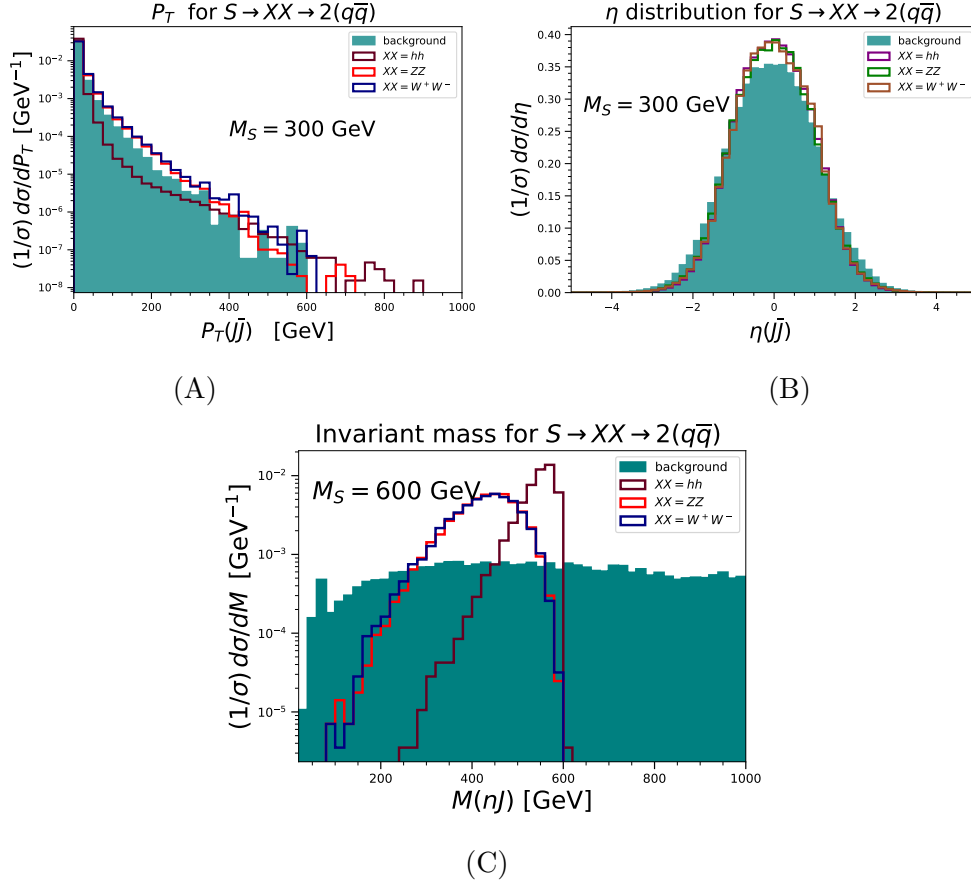


Figure 10. Plots in (A) and (B) show the transverse momentum and pseudorapidity distributions for the paired jets in final states for the signal at $M_S = 300$ GeV coming from $S \rightarrow hh, ZZ, W^+W^-$, as well as for the background. Subplot (C) shows the invariant mass $M(nj)$ for jets originated from h, Z, W^\pm decays respectively at $M_S = 600$ GeV.

event, we defined $P = \sum_{i=1}^n p(J_i)$, that sums all the jets to a single four vector, from which we construct $M^2(nj) = P^2$. This, still, will not add up to the parent S particle mass, as some of the energy will have escaped in the form of radiation, but this could be neglected as a similar effect will also be found in background events. The main effect of this final-state radiation is a shift in $M(nj)$ towards lower values, as evident in Fig. 10 (C), which was taken into account in the analysis by setting a loose $M(nj)$ interval cut. An event was accepted if its jets invariant mass was in the range $0.55 M_S \leq M(nj) \leq 1.05 M_S$ for the ZZ, WW channels and $0.8 M_S \leq M(nj) \leq 1.05 M_S$ for the hh channel. Based on Fig. 10 (C), the hh channel accepted range was adopted to be narrower compared to that of the ZZ, WW channels. Most likely, this is because jets coming from a Higgs boson's decay are produced more collinearly, and hence lose less energy in the form of radiation. This fact is supported by examining in Fig. 10 (A), that shows the tendency of jet pairs coming from the Higgs boson's decay to accumulate towards lower P_T values in comparison to those coming from WW, ZZ . Since jets in both cases (signal and backgrounds) arise either

M_S [GeV]		300	500	750	1000
$ZZ \rightarrow 2(q\bar{q})$	P_T [GeV]	6 : 376	5 : 445	5 : 265	5 : 205
	$ \eta $	< 1.75	< 1.75	< 1.25	< 1.05
$W^+W^- \rightarrow 2(q\bar{q})$	P_T [GeV]	5 : 375	5 : 305	5 : 175	5 : 185
	$ \eta $	< 2.25	< 1.65	< 1.35	< 1.05
$hh \rightarrow 2(q\bar{q})$	P_T [GeV]	-5 : 55	5 : 25	5 : 25	5 : 25
	$ \eta $	- < 3.95	< 2.15	< 1.15	< 1.065

Table 4. Samples of transverse momentum and pseudorapidity cuts for the different $4q$ channels, automated at each value of the scalar mass.

due to weak gauge bosons or the Higgs boson, which have approximately similar masses, then applying a di-jet invariant mass cut around the mediator’s mass will not help much in suppressing the background, except for the case of jets coming from W^+W^- , which yielded better efficiency for signal separation when applying $0.4M_W \leq M(J\bar{J}) \leq 1.5M_W$, with $P_T(J, \bar{J}) \geq \frac{1}{5}M_W$. The events passing the $M(nJ)$ cut were then used to build all the possible jet pairs, and the event is accepted at the end if it contains at least two jet pairs.

The surviving events were then further filtered using transverse momentum and pseudorapidity constraints via direct comparison of signal events to the background events, as illustrated in Fig. 10 (A,B). Bins of transverse momentum, P_T , were selected such that $N_s \geq 1.02N_b$ for the ZZ, hh channels and $N_s \geq 1.4N_b$ for the WW channel. The η bins were selected by requiring $N_s \geq 1.4N_b$ for both ZZ, hh channels, and $N_s \geq 1.5N_b$ for the WW channel.

These combined cuts led to an overall signal efficiency above 35% on average for all signal channels and below 10% on average for the backgrounds. The cuts were automated based on the M_s value, as shown in Table 4. Furthermore, the uncertainties in the signal and background efficiencies ($\varepsilon_s, \varepsilon_b$) were computed using Eq. 4.2, by repeating the previous analysis for different $M(nJ)$ ranges, as this represents the most critical cut in this analysis. For the second analysis, we chose a wider range for the invariant mass, $0.45M_s \leq M(nJ) \leq 1.1M_s$ for the ZZ, WW channels and $0.75M_s \leq M(nJ) \leq 1.1M_s$ for the hh channel, which led to the uncertainty in the exclusion curves shown in Fig. 11 for a luminosity of 10^4 fb^{-1} .

4.4 $2l2q$ Final States

The $2l2q$ channel is also exclusively produced by $S \rightarrow ZZ$. All possible backgrounds were generated in **MG5_aMC** via $\mu^+\mu^- \rightarrow \mu^+\mu^-l^+l^-q\bar{q}$. As in the previous channels, the most crucial distinction between signal and background is the invariant mass, which separates the resonant production from the background.

On the leptonic side, we required $P_T(l^\pm) \geq \frac{1}{5}M_Z$, based on a direct comparison of the transverse momentum of single leptons, to guarantee that we did not lose any possible leptons resulting from Z decays. Then, we paired the same-flavour oppositely charged

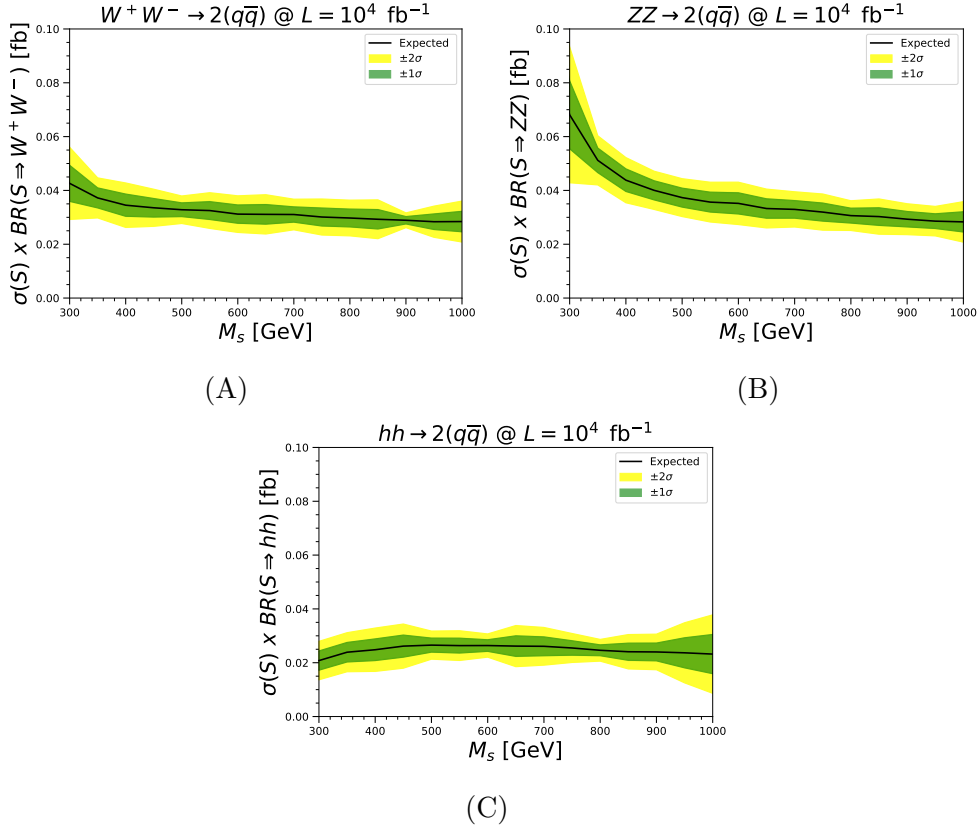


Figure 11. The sensitivity plots for (A) $S \rightarrow (WW, ZZ, hh) \rightarrow 4J$, (B) $S \rightarrow ZZ \rightarrow 4J$, and (C) $S \rightarrow W^+W^- \rightarrow 4J$, shown with the 68% and 95% C.L. intervals.

leptons if their invariant mass satisfied $0.75M_Z \leq M(l^+l^-) \leq 1.25M_Z$. Similarly, on the jet side, we asked for $0.4M_Z \leq M(nJ) \leq 1.5M_Z$, and then paired jets according to their transverse momentum $P_T(J) \geq \frac{1}{5}M_Z$, which is also confirmed from single $P_T(J)$ comparison between signal and background. We then look for resonant production around the scalar mass by computing the invariant mass of all possible combinations of the accepted (l^+l^-) pairs, together with all the accompanying jets (nJ) in each event using the formula,

$$M^2(l^+l^- + nJ) = \left(\sum_{i=1}^3 (p(l_i^+) + p(l_i^-)) + \sum_{k=1}^n p(J_k) \right)^2 \quad (4.3)$$

$$= \left(P(J) + \sum_{i=1}^3 p(l_i^+) + p(l_i^-) \right)^2, \quad (4.4)$$

such that $P(J) = \sum_k p(J_k)$ is the previously defined four vectors that add up all the jets present in a single event. This approach returned the correct invariant mass, which shifted towards lower mass values because of the unavoidable final-state radiation, especially toward higher M_s values, as depicted in Fig. 12 (C). The same figure also suggests a selection range of $M_s - 150 \text{ GeV} \leq M(l^+l^- + nJ) \leq M_s + 10 \text{ GeV}$. The event is then selected if it contains at least one combination that passes the $M(l^+l^- + nJ)$ cut and has at

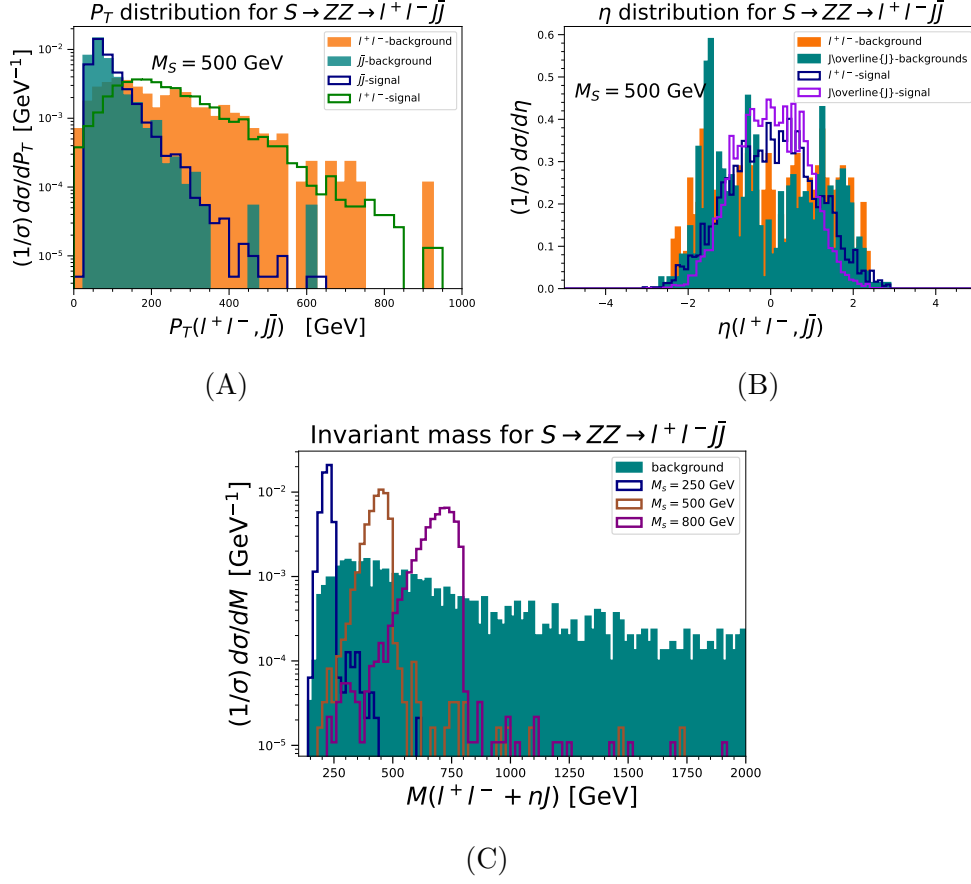


Figure 12. Plots in (A) and (B) show the transverse momentum and pseudorapidity comparisons between signal and background for $M_S = 500$ GeV. (C) shows the invariant mass $M(l^+l^- + nJ)$ obtained from Eq. (4.4) for $M_S = 250, 500, 800$ GeV.

M_S [GeV]		250	500	750	1000
Leptons	P_T [GeV]	6 : 346	19 : 689	46 : 686	67 : 657
	$ \eta $	< 2.25	< 1.65	< 2.35	< 2.35
Jets	P_T [GeV]	28 : 568	37 : 607	34 : 584	41 : 591
	$ \eta $	< 2.15	< 1.35	< 1.75	< 1.85

Table 5. Samples of transverse momentum and pseudorapidity cuts for the $2l2q$ channel, automated for each value of the scalar mass.

least one l^+l^- pair and one $(J\bar{J})$ pair passing the previous $M_Z(l^+l^-, nJ), P_T(l^+l^-, J\bar{J})$ constraints. Following the invariant mass cuts, the remaining events were subjected to cuts on $P_T(l^+l^-, J\bar{J}), \eta(l^+l^-, J\bar{J})$, through direct comparison between the signal and background for each specific M_s value, as shown in Fig. 12 (A,B) for $M_s = 500$ GeV. The P_T bins for this channel were selected by requiring $N_s \geq 2N_b$, and $N_s \geq 1.8N_b$ for the pseudorapidity (η) bins.

These bins fluctuate from M_s value to another, as shown in Table 5. These cuts led to significant suppression of the background, where $\varepsilon_b \sim 3\%$ on average and $\varepsilon_s \sim 35\%$ for the signal.

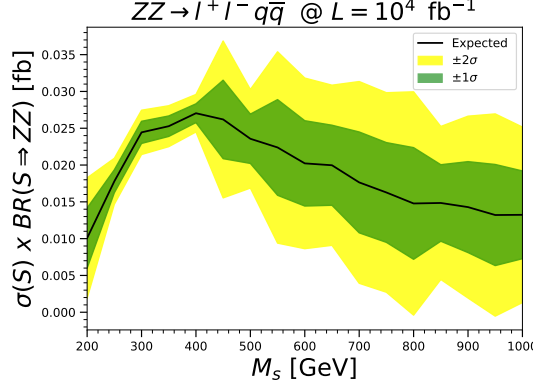


Figure 13. Sensitivity curves at $L = 10^4 \text{ fb}^{-1}$ and $\sqrt{s} = 3 \text{ TeV}$ for $S \rightarrow l^+ l^- 2J$ channel at a muon collider with 68% and 95% CL intervals.

The fluctuations in $P_{T,\eta}$ were then considered according to Eq. 4.2, by repeating the previous analysis for different invariant mass ranges $M_s - 250 \text{ GeV} \leq M(l^+ l^- + nJ) \leq M_s + 20 \text{ GeV}$ which led to the sensitivity curve for this channel, plotted in Fig. 13 at $L = 10^4 \text{ fb}^{-1}$.

4.5 $2\gamma 2q$ Final States

This final state arises from the $S \rightarrow h_1 h_1$ decay channel in addition to all the different, nonresonant background channels that lead to the same final state at the muon collider ($\mu^+ \mu^- \rightarrow \mu^+ \mu^- 2\gamma 2J$), which was generated in MG5_aMC. This channel is very challenging due to the difficulty in reconstructing both photons and jets in the final state, since a considerable number of photons would be present from the muon and quark QED radiation.

As before, the main difference between the signal and background is the absence of resonant production in the background, which suggests invariant mass cuts on the final state as an effective probe to identify the signal. Photons resulting from the Higgs boson decay could be separated from photons resulting from other decay modes, or initial/final-state radiation, by requiring $P_T(\gamma) \geq \frac{2}{5} M_h$, which was confirmed through direct comparison of the transverse momentum distributions. Then, to pair photons, we computed the invariant mass of all the possible combinations of the photons that passed the P_T cut, and only kept the pairs that had $0.8 M_h \leq M(\gamma\gamma) \leq 1.2 M_h$. We then computed the invariant mass of the

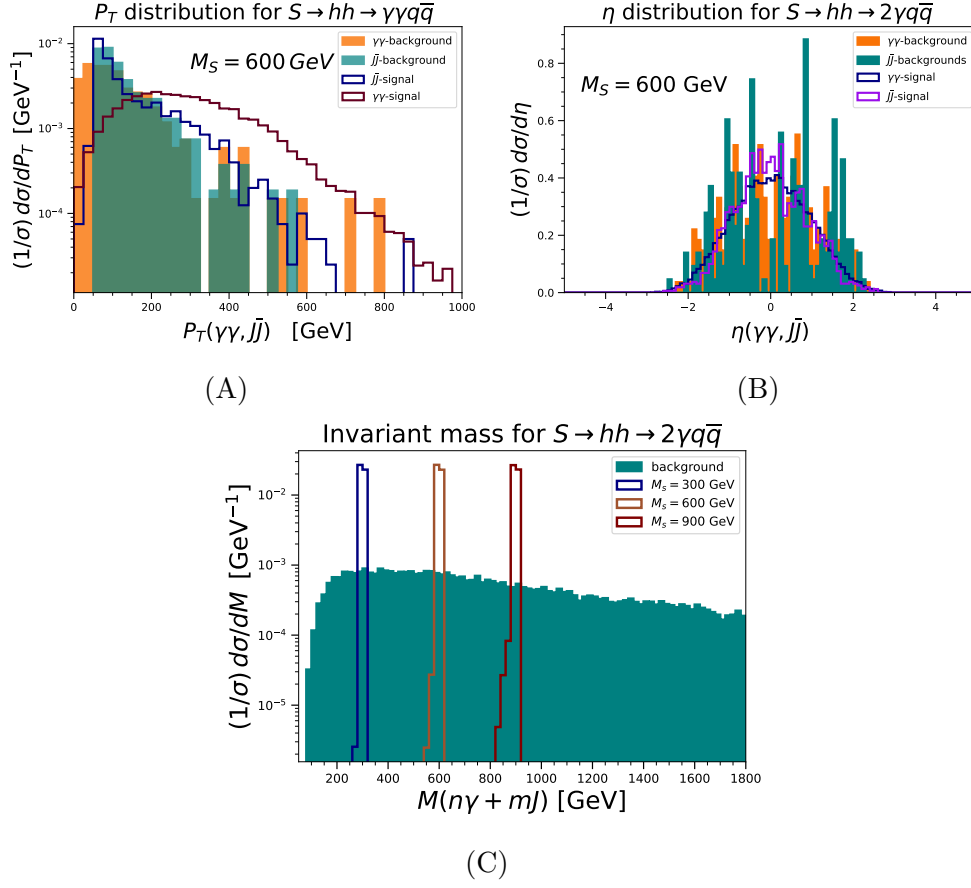


Figure 14. Subplots (A) and (B) show the transverse momentum and pseudorapidity comparisons between signal and background for $M_S = 600$ GeV, while (C) shows the invariant mass obtained from Eq. (4.6) for different M_s values.

selected photon pairs and all jets contained in the event, $M(\gamma\gamma + nJ)$, given by,⁶

$$M^2(\gamma\gamma + nJ) = \left(p(\gamma\gamma) + \sum_{k=1}^n p(J_k) \right)^2, \quad (4.5)$$

$$= P^2(\gamma\gamma + nJ), \quad (4.6)$$

where $p(\gamma\gamma) = p(\gamma_1) + p(\gamma_2)$, represents the summed vector of the photon pairs, which returns very precise peaks around the parent M_s value, as shown in Fig. 15 (C). The event was accepted if it had $M_s - 80 \text{ GeV} \leq M(\gamma\gamma + nJ) \leq M_s + 80 \text{ GeV}$, and contained at least one accepted $\gamma\gamma$ pair. Subsequently, jet pairs were constructed for all possible combinations of the remaining jets after the $P_T(J) \geq \frac{2}{5}$ constraint was applied.

The accepted events were further subjected to transverse momentum and pseudorapidity constraints, obtained through a direct comparison between the remaining signal and background events, as shown in Fig. 14 (A,B), for $M_s = 600$ GeV. We automated these cuts

⁶This is a modification of Eq. (4.4), where we take into account all the possible combinations of the accepted $\gamma\gamma$ pairs with the entire n -jets available in the event.

M_S [GeV]		300	500	750	1000
Photons	P_T [GeV]	5 : 355	6 : 476	7 : 457	6 : 446
	$ \eta $	< 2.25	< 2.15	< 2.25	< 2.15
Jets	P_T [GeV]	7 : 747	14 : 684	7 : 877	26 : 826
	$ \eta $	< 1.45	< 1.35	< 2.35	< 1.55

Table 6. Samples of transverse momentum and pseudorapidity cuts for the $2l2q$ channel, automated for each value of the scalar mass.

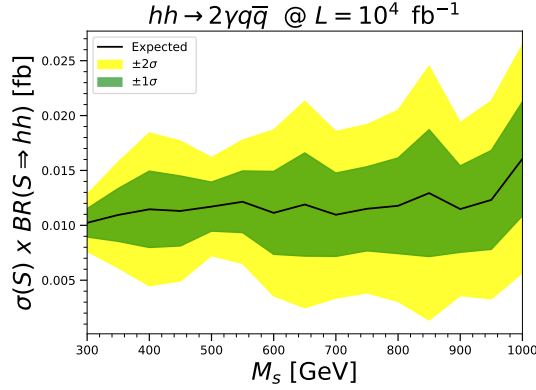


Figure 15. The sensitivity curve at $L = 10^4 \text{ fb}^{-1}$ and $\sqrt{s} = 3 \text{ TeV}$, for the $S \rightarrow 2\gamma 2J$ channel at a muon collider with 68% and 95% CLs interval.

to make them sensitive to the M_S value, as shown in Table 6. The P_T bins were obtained by requiring $N_s \geq 1.1N_b$, while $N_s \geq 1.01N_b$ was adopted for pseudorapidity (η). These observables are, in turn, dependent on the invariant mass, $M(\gamma\gamma+nJ)$, cut applied, so we repeated the above analysis for a different range, $M_s - 150 \text{ GeV} \leq M(\gamma\gamma+nJ) \leq M_s + 100 \text{ GeV}$, and computed the resulting uncertainty in the signal and background efficiencies ($\varepsilon_s, \varepsilon_b$) using Eq. (4.2). This set of cuts significantly suppressed the background, where the background efficiency was $\varepsilon_b \sim 1\%$, compared to the signal efficiency of $\varepsilon_s \sim 50\%$ on average. These results were reflected in the characteristic sensitivity curve for the $2\gamma 2q$ -channel as plotted in Fig. 15 at a luminosity of 10^4 fb^{-1} .

4.6 $2l2\nu_l$ Final states

The $2l2\nu_l$ final state can originate either from the S decay into weak gauge bosons $S \rightarrow ZZ, W^+W^-$, or other backgrounds that can be generated at a muon collider through $\mu^+\mu^- \rightarrow \mu^+\mu^-(\nu_\mu\bar{\nu}_\mu)2l2\nu_l$, and all were considered in our analysis. The invariant mass of such final states is not immediately calculable, because of the missing energy carried away by neutrinos. However, unlike in hadron colliders, the energy of the muon beam used in scalar production can be precisely estimated, giving us an opportunity to reconstruct the parent particle's mass, emphasizing one of the advantages of muon colliders over hadron colliders.

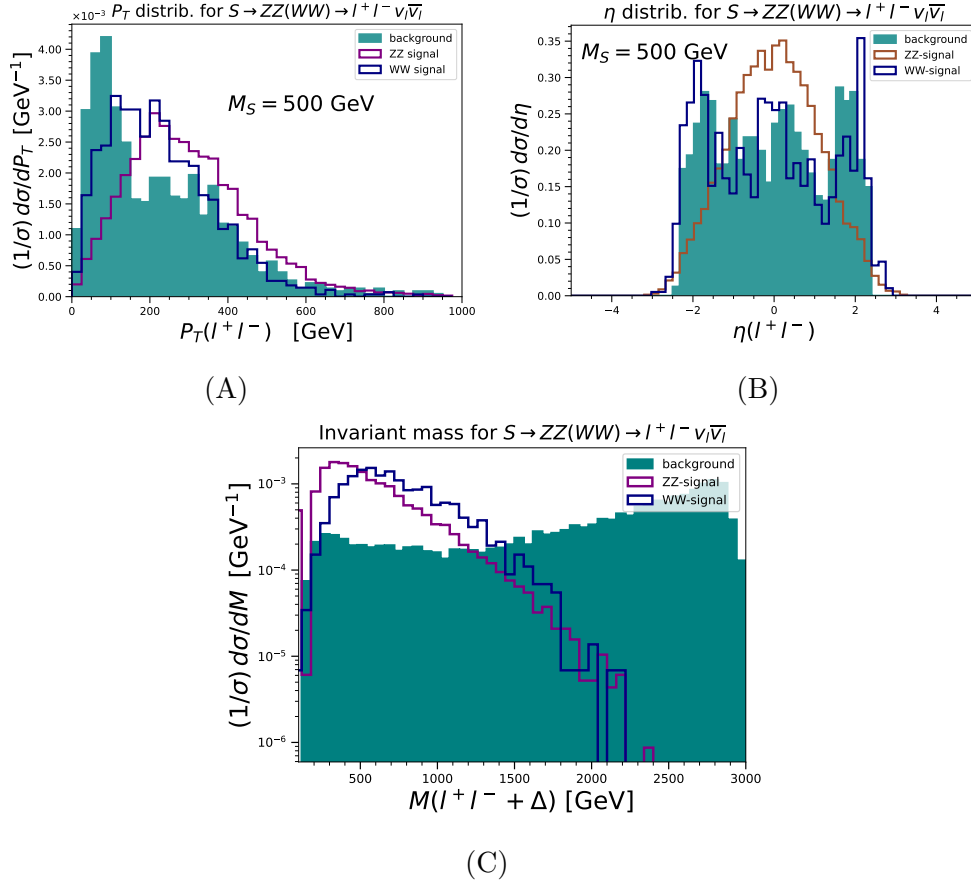


Figure 16. Subplots (A), (B) show the transverse momentum and pseudorapidity comparisons between signal and background for Z and W decays respectively, for $M_S = 500$ GeV. Subplot (C) shows the invariant mass from $2l2\nu_l$ -channel for $M_S = 600$ GeV.

The kinematics of a typical ZZF to $2l2\nu_l$ state can be derived from the Feynman diagram in Fig. 17 as follows:

$$\sqrt{s} = (q_1 + q_2 + q_3 + q_4) + (k_1 + k_2). \quad (4.7)$$

We define $\Delta = (k_1 + k_2)$, as the invariant mass of the X particle. Δ can then be easily evaluated from the muon beam energy and detected charged leptons. In other words, Δ would be a function of all four visible leptonic vectors, $\Delta(s, q_1, q_2, q_3, q_4)$. Then $\Delta \neq 0$ signifies the existence of missing energy, and the scalar mass is given by

$$M_s = M(l^+l^-) + \Delta(s, q_1, q_2, q_3, q_4), \quad (4.8)$$

where $M(l^+l^-)$ is the invariant mass of the two oppositely charged leptons. In the case of ZZF, the l^+l^- pair will originate from a single Z -boson, so only pairs with $0.8M_Z \leq M(l^+l^-) \leq 1.2M_Z$ were accepted. For WWF, l^+ and l^- will originate from different particles, that is, W^+, W^- respectively, and therefore $M(l^+l^-)$ is not expected to peak around the M_W mass. Despite this, we found that the signal from WWF tends to outnumber the

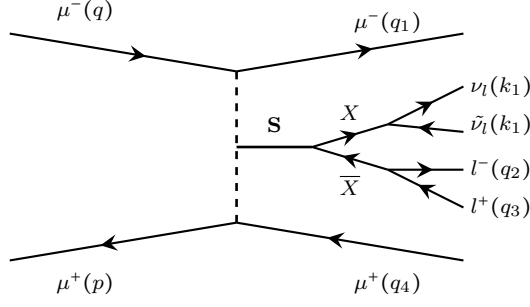


Figure 17. Feynman diagram of ZZF to $2l2\nu_l$.

M_S [GeV]		250	500	750	1000
$ZZ \rightarrow 2l2\nu_l$	P_T [GeV]	7 : 627	7 : 797	13 : 803	67 : 827
	$ \eta $	< 2.35	< 2.35	< 2.35	< 2.35
$W^+W^- \rightarrow 2l2\nu_l$	P_T [GeV]	26 : 726	126 : 506	85 : 595	45 : 725
	$ \eta $	< 2.35	< 2.35	< 2.35	< 2.35

Table 7. Samples of transverse momentum and pseudorapidity cuts for the $2l2\nu_l$ channel automated for each value of the scalar mass.

background in the region $250 \text{ GeV} \leq M(l^+l^-) \leq 600 \text{ GeV}$. In both cases, ZZF and WWF, only leptons with $P_T(l^\pm) \geq \frac{1}{5}M_X$ were included in pair formation. In this way, it is most likely that leptons included are those resulting from mediator (X) decay. However, a fraction of forward muons may satisfy these requirements. Therefore, a peak is expected to occur at $m_{ij} \sim \sqrt{s}$. However, this is not of interest to us, since we are already limiting $M_S \in [200, 1000] \text{ GeV}$, and consequently such peaks will automatically be cut out (see Fig. 16 (C)). We accepted events that had $0.6M_X \leq M(l^+l^- + \Delta) \leq 1.2M_X$ due to the broadening of the resulting invariant mass distributions observed in Fig. 16 (C).

The accepted events up to this point were further constrained by applying cuts on $P_T(l^+l^-), \eta(l^+l^-)$, from a signal-background comparison, automated for each M_s value as shown in Fig. 16 (A,B) for $M_s = 500 \text{ GeV}$. The results are shown in Table 7 for a sample of different M_s values. The P_T bins were selected by requiring $N_s \geq 1.2N_b$ and $N_s \geq 1.1N_b$ for the η bins for the ZZ, WW channels. Similarly to the previous channels, the uncertainty in $\varepsilon_s, \varepsilon_b$ was computed from Eq. (4.2), by repeating the previous analysis for different invariant mass range, $0.5M_X \leq M(l^+l^- + \Delta) \leq 1.3M_X$.

The full analysis yielded a background efficiency of $\varepsilon_b \sim 4\%$ against a signal efficiency of $\varepsilon_s \sim 40\%$ for $ZZ \rightarrow 2l2\nu_l$. Instead, for the $WW \rightarrow 2l2\nu_l$ final state, the results were not as good, because the leptons did not originate from the same particle, which led to a less efficient signal-background separation. This is reflected in the sensitivity plots in Fig. 18, which show a more uncertain curve for the WW channel compared to the ZZ channel.

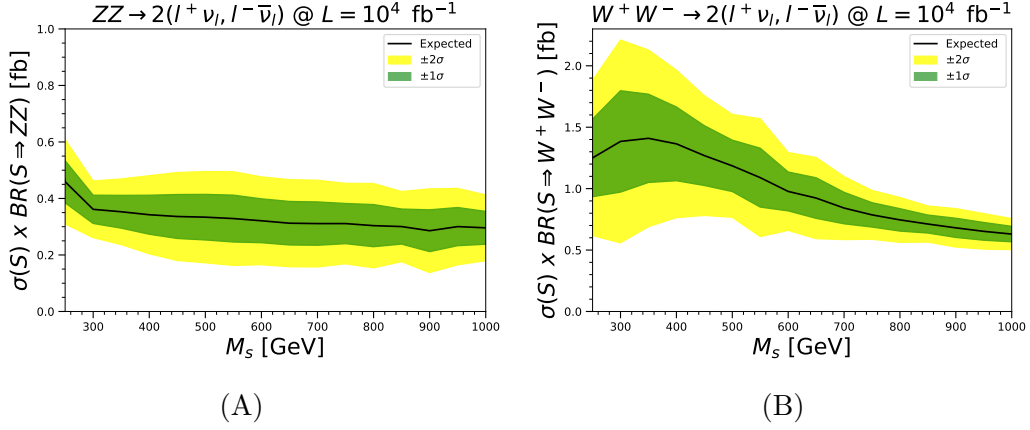


Figure 18. (A) and (B) show the sensitivity curves at $L = 10^4 \text{ fb}^{-1}$ and $\sqrt{s} = 3 \text{ TeV}$ for $S \rightarrow ZZ \rightarrow 2l2\nu_l$ and $S \rightarrow W^+W^- \rightarrow 2l2\nu_l$ channels respectively at a muon collider with 68% and 95% CLs intervals.

$M_S \text{ [GeV]}$	250	500	750	1000
$P_T(J\bar{J}) \text{ [GeV]}$	9 : 979	5 : 1185	5 : 1105	5 : 1205
$ \eta(J\bar{J}) $	< 0.55	< 2.45	< 2.65	< 2.75

Table 8. Samples of transverse momentum and pseudorapidity cuts for the $2q2\nu_l$ channel, automated for each value of the scalar mass.

4.7 $2q2\nu_l$ Final states

Unlike in the $2l2\nu_l$ case, this final state can originate from the S decay into Z -bosons, $S \rightarrow ZZ$, together with all possible backgrounds resulting from $\mu^+\mu^- \rightarrow \mu^+\mu^-(\nu_\mu\bar{\nu}_\mu)2q2\nu_l$. Similarly to the previous channel, it would be impossible to directly compute the invariant mass owing to the missing energy carried away by the neutrinos. However, we can employ the same formula as Eq. (4.8) to evaluate it, with a slight replacement of $l^+l^- \rightarrow nJ$, where all the jets contained in the event are sourced from a single Z boson, and Δ becomes a function of the forward muons (q_1, q_2) and all the jets (p_1, p_2, \dots, p_n).

Therefore, the invariant mass in this case is given by

$$M(nJ + \Delta) = M(nJ) + \Delta(s, q_1, q_2, p_1, p_2, \dots, p_n). \quad (4.9)$$

This formula correctly returns a resonant peak around each M_s value, as shown in Fig. 19 (C) for $M_s = 250, 550, 750 \text{ GeV}$. Figure 19 (C) also suggests an invariant mass range of $.9M_s \leq M(nJ + \Delta) \leq 1.5M_s$ to separate the signal from the background.

In order to accept an event, we further require that it must contain at least one jet pair, $J\bar{J}$, with $0.5M_Z \leq M(J\bar{J}) \leq 1.4M_Z$ for $P_T(J, \bar{J}) \geq \frac{1}{5}M_Z$. We then applied cuts on $P_T(J\bar{J}), \eta(J\bar{J})$, obtained through a direct signal-background comparison, as shown in Fig. 19 (A,B) for $M_s = 550 \text{ GeV}$. These secondary cuts were automated for each M_s value, as illustrated in Table 8 for a sample of selected M_s values. The P_T bins were selected by

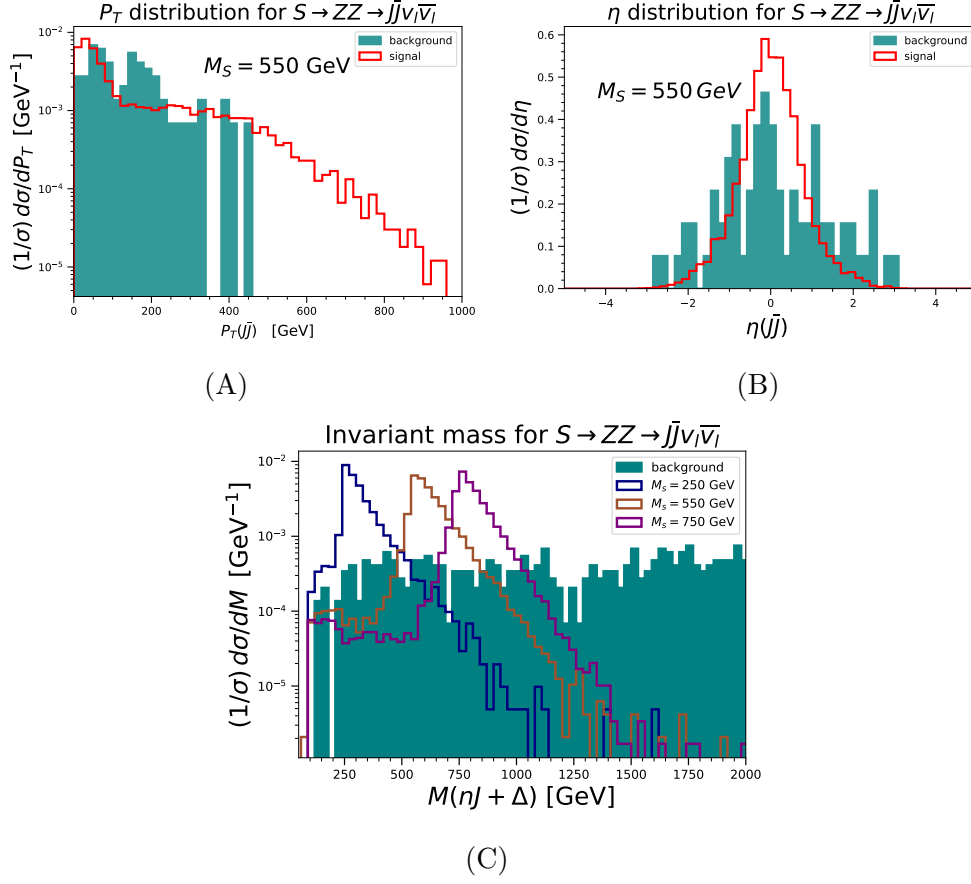


Figure 19. Subplots (A), (B) show the transverse momentum and pseudorapidity comparisons between signal and background for $M_S = 550$ GeV. Subplot (C) shows the invariant mass obtained for $M_S = 250, 550, 750$ GeV.

requiring $N_s \geq 1.2N_b$ and $N_s \geq 1.4N_b$ for the η bins. Similarly to all previous channels, the uncertainty in $\varepsilon_s, \varepsilon_b$ was computed using Eq.(4.2) by repeating the preceding analysis for a different invariant mass range, $0.85M_X \leq M(l^+l^- + \Delta) \leq 1.6M_X$.

This analysis scheme greatly suppressed the background, yielding a background efficiency of $\varepsilon_b \sim 1\%$ on average, while the signal efficiency ε_s exceeded 25% on average. The corresponding sensitivity plot for this final state is shown in Fig. 20 for a luminosity of $L = 10^4 \text{ fb}^{-1}$.

4.8 $l\nu_l 2q$ Final states

This final state is another gauge boson-initiated channel that arises only from $S \rightarrow W^+W^- \rightarrow l^+\nu_l(l^-\tilde{\nu}_l)q\bar{q}$. All backgrounds contributing to this channel that could be generated at the muon collider from $\mu^+\mu^- \rightarrow mu^+\mu^-l^+\nu_l(l^-\tilde{\nu}_l)q\bar{q}$ were considered. The invariant mass of the fully visible final states can also be evaluated using Eq. 4.8, but now ‘ Δ ’ will be a function of an extra lepton vector (i.e. p_3) which results from W -boson decay,

$$M_s = M(l^\pm + nJ) + \Delta(s, q_1, q_2, q_3, p_1, p_2, \dots p_n), \quad (4.10)$$

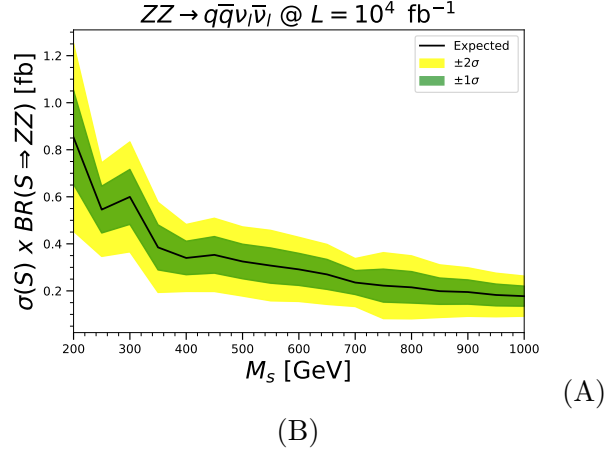


Figure 20. The sensitivity curves at $L = 10^4 \text{ fb}^{-1}$ and $\sqrt{s} = 3 \text{ TeV}$ for $S \rightarrow ZZ \rightarrow 2q2\nu_l$ at a muon collider with 68% and 95% CLs intervals.

$M_S \text{ [GeV]}$		250	500	750	1000
$W^+W^- \rightarrow l^\pm \nu_l (\bar{\nu}_l) q\bar{q}$	$P_T(l^\pm) \text{ [GeV]}$	111 : 361	111 : 311	91 : 331	81 : 371
	$ \eta(l^\pm) $	2 : 2.45	2.1 : 2.45	< 2.45	< 2.45
	$P_T(J\bar{J}) \text{ [GeV]}$	39 : 509	409 : 469	32 : 612	35 : 725
	$ \eta(J\bar{J}) $	< 2.25	< 1.95	< 1.65	< 1.65

Table 9. Samples of transverse momentum and pseudorapidity cuts for the $2q2\nu_l$ and $l\nu_l 2q$ channels, automated for different values of the scalar mass.

where ‘ q_1, q_2, q_3 ’ are the four vectors of the two forward muons and extra lepton resulting from one W^\pm -boson decay. ‘ p_1, p_2, \dots, p_n ’ are the entire n -jets four vectors in the event.

$M(l^\pm + nJ)$ runs over all possible combinations of a single charged lepton in the final state, with n jets available in the event. This includes forward high-energy scattered muons, so a secondary peak around $M_S \approx \sqrt{s}$ should be expected, and could be ignored for the reasons discussed earlier. In fact, this will not even be seen in this case because the jets largely outnumber the forward muons, and hence the secondary peak at $M_S = \sqrt{s}$ will be smeared away, which would be further enhanced by only considering charged leptons with $P_T(l^\pm) \geq \frac{1}{5}M_W$ that shall suppress the forward muon contributions. This approach generated well-defined invariant mass distributions for all the examined M_s values, as can be seen in Fig. 21 (C), which suggests a narrower invariant mass range compared to the previous channel, $0.85M_s \leq M(l^\pm + nJ + \Delta) \leq 1.5M_s$. If the event passes this primary cut, we then check whether the jet invariant mass peaks around the W -boson mass, $0.75M_W \leq M(nJ) \leq 1.25M_W$. If it does, then we construct all possible jet pairs with $P_T \geq \frac{1}{5}M_W$. At least one pair of jets, $J\bar{J}$, is required in order to pass this event to the secondary analysis. In this step, we check for the observables $P_T(J\bar{J}), \eta(J\bar{J})$, the regions

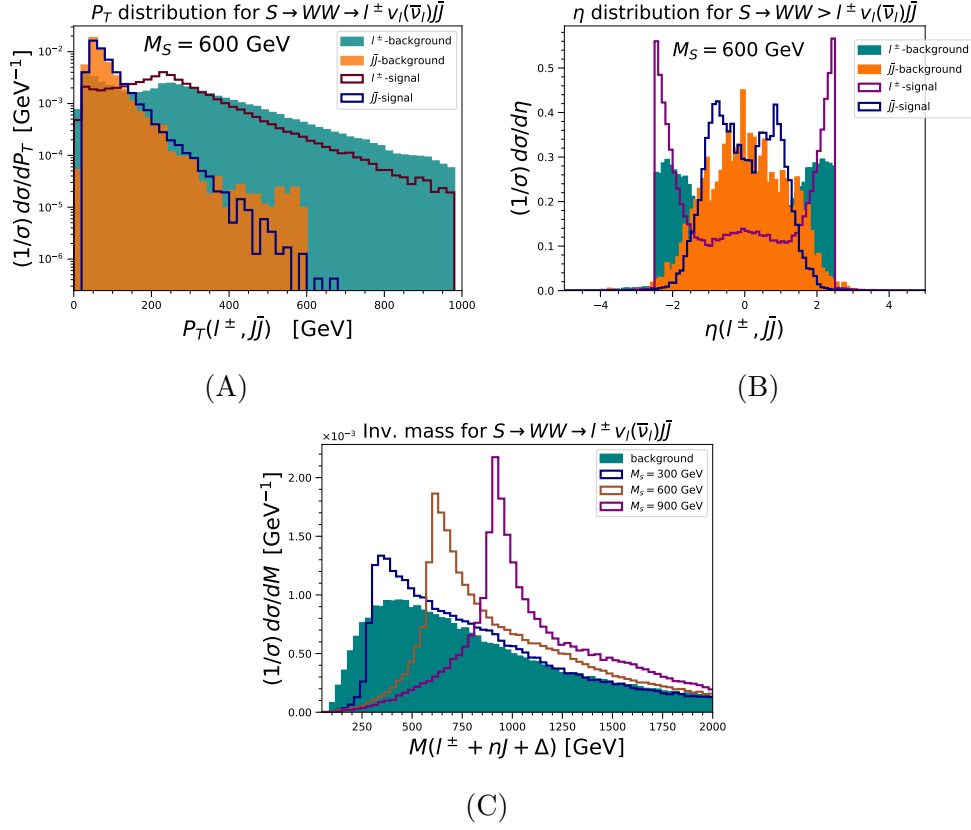


Figure 21. (A) and (B) show the transverse momentum and pseudorapidity distributions of paired jets and a single charged lepton obtained from $l\nu_l 2q$ -channel for $M_S = 600$ GeV. (C) shows the invariant mass distributions of $l\nu_l 2q$ -channel for $M_S = 300, 600, 900$ GeV.

where the signal outnumbers the background, keeping only the bins where $N_s \geq 1.1N_b$ for $P_T(J\bar{J})$ and $N_s \geq 1.2N_b$ for $\eta(J\bar{J})$. This scanning procedure is automated for each M_s value as shown in Fig. 21 (A,B) for $M_s = 600$ GeV, and for other different scalar mass values in Table 9. We finally account for the fluctuations in the measured efficiencies by repeating the previous analysis for a different invariant mass range, $0.8M_s \leq M(l^\pm + nJ + \Delta) \leq 1.65M_s$, and then compute $U(\sigma_s)$ using Eq. (4.2).

Our analysis successfully suppressed backgrounds in comparison to signal events, with $\varepsilon_b \sim 10 : 40\%$, and $\varepsilon_s \sim 25 : 88\%$. This channel shows a sensitivity in $\varepsilon_s, \varepsilon_b$ to the scalar mass value, as both tend to grow for higher M_s values, a feature that was not observed in the other channels. This feature is reflected in the sensitivity plot in Fig. 22, where the uncertainty in the signal cross section converges towards higher values of the scalar mass as ε_s becomes larger than 50%, which guarantees that the uncertainties will be smaller.

5 Results

Using the phenomenological analyses described above, we explored the parameter space points that fulfill the SFOEWPT conditions using the derived sensitivity plots, as illus-

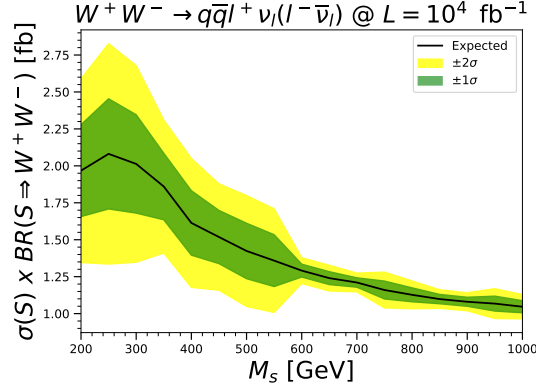


Figure 22. Sensitivity curves for $S \rightarrow l\nu_l 2q$ at a muon collider with $L = 10^4 \text{ fb}^{-1}$ and $\sqrt{s} = 3$ with 68% and 95% C.L. intervals.

trated in Fig. 23. It is evident that channels containing quarks in the final state can explore

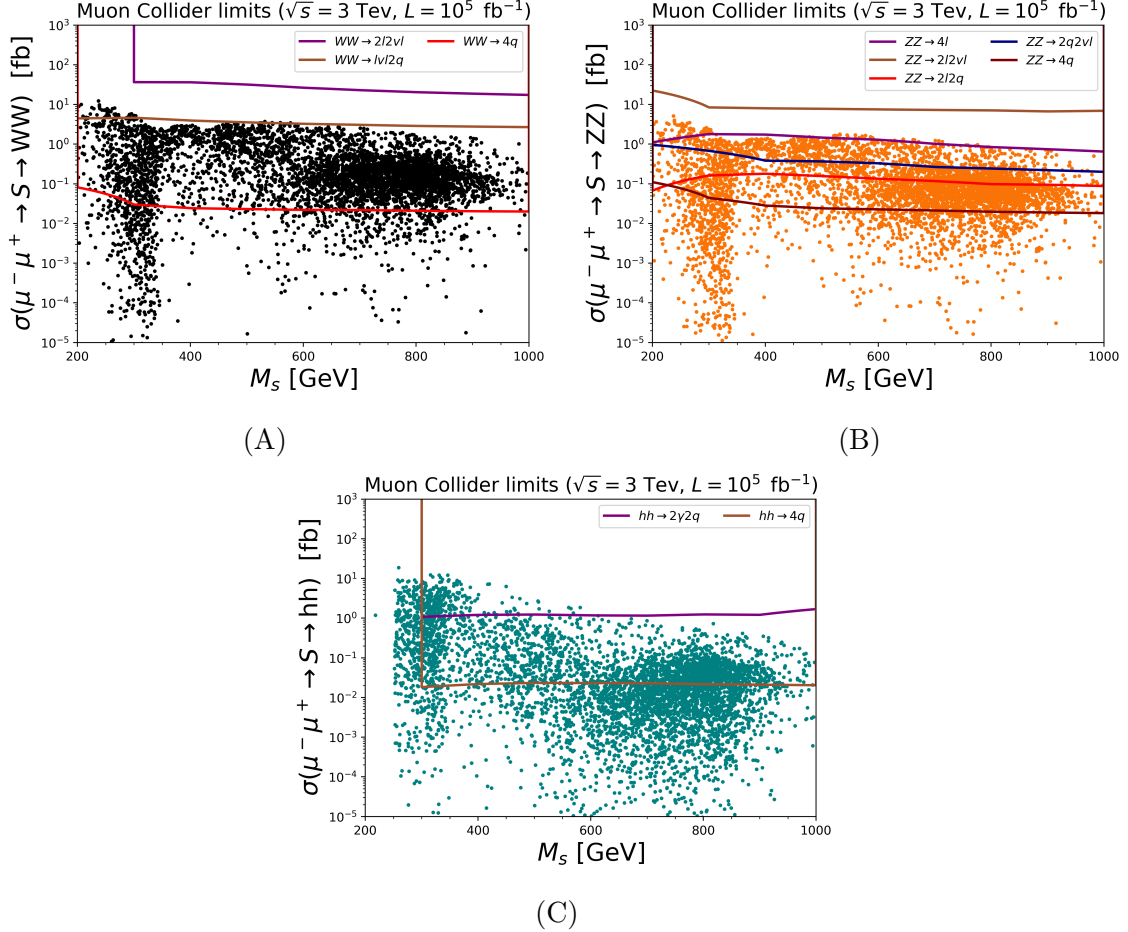


Figure 23. Exclusion curves for all channels from $S \rightarrow WW, ZZ, hh$ respectively at a muon collider with $\sqrt{s} = 3 \text{ TeV}$ and $L = 10^5 \text{ fb}^{-1}$.

a larger portion of the xSM SFOEWPT parameter space. This is primarily attributed to the higher branching ratios of the Higgs bosons and vector bosons to the jets. The relative absence of substantial QCD backgrounds at a muon collider, in comparison to hadron colliders, enables the reconstruction of jets via a comparatively straightforward approach. This factor facilitates efficient background suppression, even for channels with invisible final states. This same rationale supports the pursuit of potential precision tests of the Higgs boson self-couplings at a muon collider, and the possible confirmation or exclusion of the SFOEWPT scenario. We reserve such an investigation for future studies, along with the examination of potential kinematical differences between jets originating from $S \rightarrow hh$ and $S \rightarrow ZZ(WW)$, which may be related to the \mathbb{Z}_2 nature of the extended potential of the xSM.

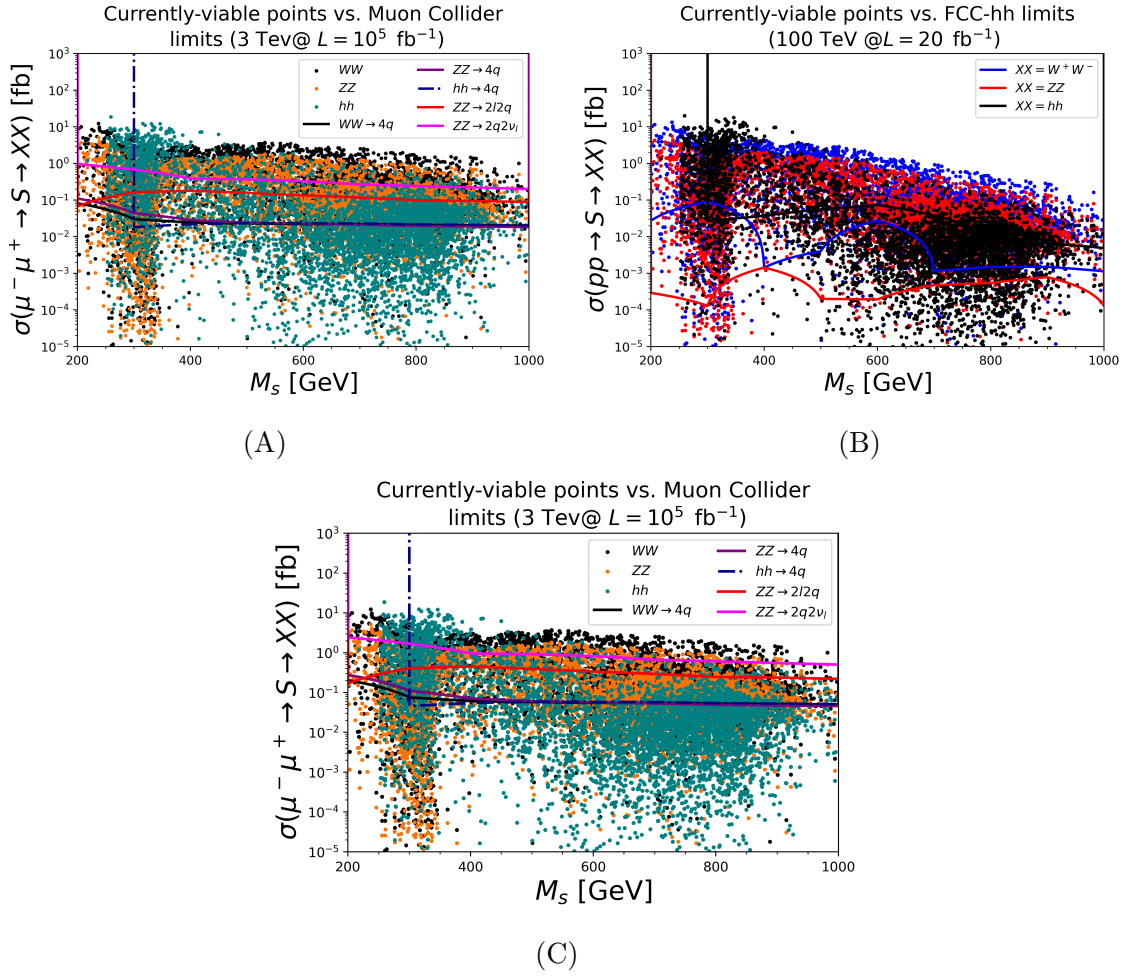


Figure 24. (A) shows the combined WW , ZZ , $hh \rightarrow nJ$ final states at a muon collider with $\sqrt{s} = 3$ TeV and $L = 10^5 \text{ ab}^{-1}$. (B) shows the FCC-hh exclusion curves for the same channels at a much higher energy $\sqrt{s} = 100$, TeV and much smaller luminosity $L = 20 \text{ fb}^{-1}$. (C) represents the discovery plot for $S = 5$.

Figure 23 presents the currently viable parameter space points that satisfy the SFOEWPT

conditions for both the liberal and conservative categories discussed in Section 2 in conjunction with the sensitivity plots obtained from the previous subsections. Figure 23 (A) summarizes all the different final states that could be obtained from WW decay, and Fig. 23 (B,C) for ZZ and hh , respectively, at a luminosity of 10^5 fb^{-1} .⁷ The preferred channels, that is, jet-rich channels, have consequently been isolated in Fig. 24, as they represent the primary limiting channels in a muon collider. Compared to the FCC-hh potential for searches, depicted in Fig. 24 (B), the muon collider appears to be capable of excluding the majority of points that could be examined at the FCC-hh at significantly lower center-of-mass energies, particularly for $S \rightarrow XX \rightarrow 4q$.

In the event of a positive detection of the real singlet at the proposed future muon collider, it will still be possible to exclude a significant portion of FOEWPT parameter space points. This accounts for a modification of the statistical significance in Eq.(4.1) from $\mathcal{S} = 2$ to $\mathcal{S} = 5$, which results in a consistent and slight upward shift of the sensitivity curves across all channels. This result is illustrated in Fig. 24 (c). From that discovery plot, we can further estimate, in the event of a positive detection, the anticipated mixing between the two scalars. As discussed in Section 3, the potential in Eq. (2.3) results in mixing between the SM Higgs and the new scalar, which is a desirable characteristic for enhancing the FOEWPT. This mixing will scale all the Higgs couplings by $\cos \theta$ [27].

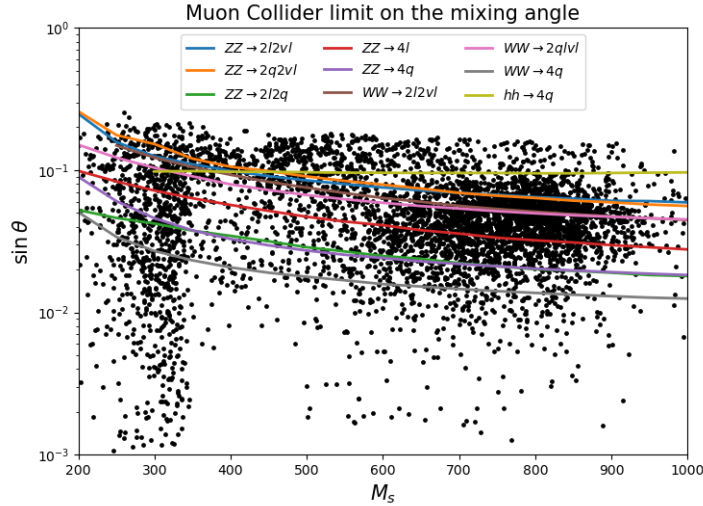


Figure 25. The limits in the Higgs-real scalar mixing extracted from the different decay channels that could be probed at the muon collider.

In Ref. [68], the authors discussed the sensitivity of the Higgs boson’s properties to new physics, particularly its couplings to weak gauge bosons, and the Higgs trilinear coupling. In this investigation, the source of the ‘new physics’ is the real singlet extension, which inevitably scales all of the Higgs boson’s couplings. Of particular importance for this study

⁷The exclusion curve is proportional to $\frac{1}{\sqrt{L}}$ (see Eq. (4.1)), so we have chosen an order of magnitude higher luminosity than the value used in the previous exclusion curves in order to explore a larger parameter space volume.

is the modification of the Higgs trilinear coupling due to this extension, given its role in governing the Higgs potential and, consequently, the type and strength of the EWPT. This work is currently in progress. However, utilizing the discovery plots in Fig. 24 (C), it is possible to extrapolate certain limits on the mixing angle between the two scalars, which may be observed in current and future precision tests of the Higgs properties. Following ref. [27], the mixing angle between the two scalars can be derived from,

$$\sin^4 \theta = \frac{\sigma_{\text{BSM}}(\mu^+ \mu^- \xrightarrow{VBF} s \rightarrow f \bar{f})}{\sigma_{\text{SM}}(\mu^+ \mu^- \xrightarrow{VBF} h \rightarrow f \bar{f})}, \quad (5.1)$$

where, σ_{BSM} represents the expected cross section obtained from our analysis in Section. 4, and σ_{SM} denotes the SM cross section for each final state topology computed using **MG5_aMC**, setting $m_h = m_s$ ($\sin \theta = 1$). Through this analysis for the muon collider, it is anticipated that $0.02 \leq \sin \theta \leq 0.15$ in the event of a positive discovery. This result can already exclude some of the valid parameter space points for FOEWPT, as each set predicts a specific value for the mixing angle, which is illustrated in Fig. 25 for both the conservative and liberal categories.

6 Conclusions

In this study, we investigated the potential of a high-energy muon collider to explore electroweak phase transitions in the context of the Standard Model extended by a real scalar singlet. Our analysis focused on examining the occurrence of a strong first-order electroweak phase transition, which is essential for explaining baryogenesis, and may result in observable gravitational waves.

As the initial step of our investigation, we identified Lagrangian parameter values for which xSM can produce a strong first-order phase transition that satisfies the sphaleron critical conditions for baryogenesis. These parameter values span a broad parameter space for the xSM. Subsequently, assuming a future muon collider with center-of-mass energy $\sqrt{s} = 3$ TeV, we assessed the sensitivity to a new scalar singlet-like particle through various final states. Our findings indicate that the muon collider can be an effective tool for probing the xSM parameter space if high luminosities can be approached, where the clean environment of a muon collider allows for precise measurements, particularly producing a scalar singlet-like particle via vector boson fusion (VBF). We primarily examined the direct production of the new scalar and its decay into all viable final states, which offers a promising avenue for its discovery or exclusion. We found that decay channels rich with jets in the final states are the most promising for excluding FOEWPT parameter space points at the muon collider. Indirectly, deviations in the Higgs boson couplings from the SM expectations could provide further evidence for the presence of a new scalar singlet-like particle, which would be valuable to explore further in the muon collider. With precision measurements, the zero-temperature part of the effective potential can be reconstructed at the muon collider, whereas gravitational wave observations can provide additional information on thermal dynamics. The scalar singlet-enhanced electroweak phase transition

can also generate a signal in gravitational wave detectors, which enables the muon collider to provide complementary information for gravitational wave detectors.

Our findings highlight the unique advantages of a muon collider in exploring electroweak symmetry breaking and potentially new physics beyond the Standard Model. The ability to resolve the nature of the electroweak phase transition in such a collider is of paramount importance, especially for advancing our understanding of early universe dynamics and the mechanisms behind baryogenesis, providing significant advancement in our understanding of electroweak symmetry breaking and its implications in cosmology.

Acknowledgments

The research of C.B. is supported by the Australian Research Council through DP210101636, DP220100643, and LE210100015. A.P. acknowledges support by the National Science Foundation under Grant No. PHY 2210161.

References

- [1] D.A. Kirzhnits and A.D. Linde, *Macroscopic consequences of the weinberg model*, *Physics Letters B* **42** (1972) 471.
- [2] S. Coleman and E. Weinberg, *Radiative corrections as the origin of spontaneous symmetry breaking*, *Physical Review D* **7** (1973) 1888.
- [3] L. Dolan and R. Jackiw, *Symmetry behavior at finite temperature*, *Physical Review D* **9** (1974) 3320.
- [4] M. Quiros, *Finite temperature field theory and phase transitions*, *Proceedings, Summer school in high-energy physics and cosmology: Trieste, Italy* **1999** (1998) 187.
- [5] R. Jackiw, *Functional evaluation of the effective potential*, *Physical Review D* **9** (1974) 1686.
- [6] S. Weinberg, *Perturbative calculations of symmetry breaking*, *Physical Review D* **7** (1973) 2887.
- [7] L. Dolan and R. Jackiw, *Gauge-invariant signal for gauge-symmetry breaking*, *Physical Review D* **9** (1974) 2904.
- [8] A.D. Sakharov, *Violation of CP Invariance, C asymmetry, and baryon asymmetry of the universe*, *Pisma Zh. Eksp. Teor. Fiz.* **5** (1967) 32.
- [9] M. Dine and A. Kusenko, *Origin of the matter-antimatter asymmetry*, *Reviews of Modern Physics* **76** (2003) 1.
- [10] D.E. Morrissey and M.J. Ramsey-Musolf, *Electroweak baryogenesis*, *New Journal of Physics* **14** (2012) 125003.
- [11] G. Bhattacharyya, *A pedagogical review of electroweak symmetry breaking scenarios*, *Reports on Progress in Physics* **74** (2011) 026201.
- [12] L. McLerran, M. Shaposhnikov, N. Turok and M. Voloshin, *Why the baryon asymmetry of the universe is 10^{-10}* , *Physics Letters B* **256** (1991) 477.
- [13] E. Senaha, *Overview of electroweak baryogenesis*, *arXiv preprint arXiv:1305.1563* (2013) .
- [14] J.M. Cline, *Baryogenesis*, *arXiv preprint hep-ph/0609145* (2006) .

- [15] S. Braibant, Y. Brihaye and J. Kunz, *Sphalerons at finite temperature*, *International Journal of Modern Physics A* **8** (1993) 5563.
- [16] A. Ahriche, *What is the criterion for a strong first order electroweak phase transition in singlet models?*, *Physical Review D—Particles, Fields, Gravitation, and Cosmology* **75** (2007) 083522.
- [17] M. Carrington, *Effective potential at finite temperature in the standard model*, *Physical Review D* **45** (1992) 2933.
- [18] J. Espinosa, M. Quiros and F. Zwirner, *On the nature of the electroweak phase transition*, *Physics Letters B* **314** (1993) 206.
- [19] P. Arnold and O. Espinosa, *Effective potential and first-order phase transitions: Beyond leading order*, *Physical Review D* **47** (1993) 3546.
- [20] K. Kajantie, M. Laine, K. Rummukainen and M. Shaposhnikov, *Is there a hot electroweak phase transition at $m_h \gtrsim m_w$?*, *arXiv preprint hep-ph/9605288* (1996) .
- [21] E. Senaha, *Symmetry restoration and breaking at finite temperature: an introductory review*, *Symmetry* **12** (2020) 733.
- [22] J.R. Espinosa, T. Konstandin and F. Riva, *Strong electroweak phase transitions in the standard model with a singlet*, *Nuclear Physics B* **854** (2012) 592.
- [23] J. Choi and R. Volkas, *Real higgs singlet and the electroweak phase transition in the standard model*, *Physics Letters B* **317** (1993) 385.
- [24] D. O’Connell, M.J. Ramsey-Musolf and M.B. Wise, *Minimal extension of the standard model scalar sector*, *Physical Review D* **75** (2007) 037701.
- [25] S. Ham, Y. Jeong and S. Oh, *Electroweak phase transition in an extension of the standard model with a real higgs singlet*, *Journal of Physics G: Nuclear and Particle Physics* **31** (2005) 857.
- [26] M.J. Ramsey-Musolf, *The electroweak phase transition: a collider target*, *Journal of High Energy Physics* **2020** (2020) 1.
- [27] A. Papaefstathiou and G. White, *The electro-weak phase transition at colliders: Discovery post-mortem*, *Journal of High Energy Physics* **2022** (2022) 1.
- [28] G. Branco, D. Delepine, D. Emmanuel-Costa and R.G. Felipe, *Electroweak baryogenesis in the presence of an isosinglet quark*, *Physics Letters B* **442** (1998) 229.
- [29] V. Barger, P. Langacker, M. McCaskey, M. Ramsey-Musolf and G. Shaughnessy, *Complex singlet extension of the standard model*, *Physical Review D—Particles, Fields, Gravitation, and Cosmology* **79** (2009) 015018.
- [30] U. Ellwanger, C. Hugonie and A.M. Teixeira, *The next-to-minimal supersymmetric standard model*, *Physics Reports* **496** (2010) 1.
- [31] M. Carena, Z. Liu and Y. Wang, *Electroweak phase transition with spontaneous z_2 -breaking*, *Journal of High Energy Physics* **2020** (2020) 1.
- [32] J.M. No and M. Ramsey-Musolf, *Probing the higgs portal at the lhc through resonant di-higgs production*, *Physical Review D* **89** (2014) 095031.
- [33] S.J. Huber and T. Konstandin, *Gravitational wave production by collisions: more bubbles*, *Journal of Cosmology and Astroparticle Physics* **2008** (2008) 022.

- [34] D. Curtin, P. Meade and C.-T. Yu, *Testing electroweak baryogenesis with future colliders*, *Journal of High Energy Physics* **2014** (2014) 1.
- [35] H. Al Ali, N. Arkani-Hamed, I. Banta, S. Benevides, D. Buttazzo, T. Cai et al., *The muon smasher's guide*, *Reports on Progress in Physics* **85** (2022) 084201.
- [36] W. Liu and K.-P. Xie, *Probing electroweak phase transition with multi-teV muon colliders and gravitational waves*, *Journal of High Energy Physics* **2021** (2021) 1.
- [37] M. Forsslund and P. Meade, *High precision higgs from high energy muon colliders*, *Journal of High Energy Physics* **2022** (2022) 1.
- [38] S. Profumo, M.J. Ramsey-Musolf and G. Shaughnessy, *Singlet higgs phenomenology and the electroweak phase transition*, *Journal of High Energy Physics* **2007** (2007) 010.
- [39] M. Laine and A. Vuorinen, *Basics of thermal field theory—a tutorial on perturbative computations*, *arXiv preprint arXiv:1701.01554* (2017) .
- [40] R.G. Leigh, *Infrared effects and bubble propagation at the electroweak phase transition*, 1992.
- [41] M. Laine and A. Vuorinen, *Basics of thermal field theory*, *Lect. Notes Phys* **925** (2016) 1701.
- [42] P. Arnold, *Phase transition temperatures at next-to-leading order*, *Physical Review D* **46** (1992) 2628.
- [43] P. Fendley, *The effective potential and the coupling constant at high temperature*, *Physics Letters B* **196** (1987) 175.
- [44] E. Fernández-Martínez, J. López-Pavón, J. No, T. Ota and S. Rosauero-Alcaraz, *ν electroweak baryogenesis: the scalar singlet strikes back*, *The European Physical Journal C* **83** (2023) 715.
- [45] A. Papaefstathiou and G. White, *The electro-weak phase transition at colliders: confronting theoretical uncertainties and complementary channels*, *Journal of High Energy Physics* **2021** (2021) .
- [46] P. Athron, C. Balázs, A. Fowlie and Y. Zhang, *Phasetracer: tracing cosmological phases and calculating transition properties*, *The European Physical Journal C* **80** (2020) 1.
- [47] A. Fowlie, *A fast c++ implementation of thermal functions*, *Computer Physics Communications* **228** (2018) 264.
- [48] C.L. Wainwright, *Cosmotransitions: computing cosmological phase transition temperatures and bubble profiles with multiple fields*, *Computer Physics Communications* **183** (2012) 2006.
- [49] M. Lewicki, M. Merchand, L. Sagunski, P. Schicho and D. Schmitt, *Impact of theoretical uncertainties on model parameter reconstruction from gw signals sourced by cosmological phase transitions*, 2024.
- [50] O. Gould and C. Xie, *Higher orders for cosmological phase transitions: a global study in a yukawa model*, 2023.
- [51] C. collaboration et al., *Search for a standard-model-like higgs boson with a mass in the range 145 to 1000 gev at the lhc*, *arXiv preprint arXiv:1304.0213* (2013) .
- [52] D. Buttazzo, D. Redigolo, F. Sala and A. Tesi, *Fusing vectors into scalars at high energy lepton colliders*, *Journal of High Energy Physics* **2018** (2018) 1.
- [53] A. Costantini, F. De Lillo, F. Maltoni, L. Mantani, O. Mattelaer, R. Ruiz et al., *Vector boson fusion at multi-teV muon colliders*, *Journal of High Energy Physics* **2020** (2020) 1.

- [54] J. Alwall, M. Herquet, F. Maltoni, O. Mattelaer and T. Stelzer, *MadGraph 5 : Going Beyond*, *JHEP* **06** (2011) 128 [[1106.0522](#)].
- [55] M. Bahr et al., *Herwig++ Physics and Manual*, *Eur. Phys. J. C* **58** (2008) 639 [[0803.0883](#)].
- [56] J. Bellm et al., *Herwig 7.1 Release Note*, [1705.06919](#).
- [57] S. Gieseke et al., *Herwig++ 2.5 Release Note*, [1102.1672](#).
- [58] K. Arnold et al., *Herwig++ 2.6 Release Note*, [1205.4902](#).
- [59] J. Bellm et al., *Herwig++ 2.7 Release Note*, [1310.6877](#).
- [60] J. Bellm et al., *Herwig 7.2 release note*, *Eur. Phys. J. C* **80** (2020) 452 [[1912.06509](#)].
- [61] G. Bewick et al., *Herwig 7.3 Release Note*, [2312.05175](#).
- [62] Papaefstathiou, Andreas, “The HwSim analysis package for HERWIG 7.”
<https://gitlab.com/apapaefs/hwsim>.
- [63] R. Brun and F. Rademakers, *ROOT: An object oriented data analysis framework*, *Nucl. Instrum. Meth. A* **389** (1997) 81.
- [64] M. Cacciari, G.P. Salam and G. Soyez, *FastJet User Manual*, *Eur. Phys. J. C* **72** (2012) 1896 [[1111.6097](#)].
- [65] S. Catani, Y.L. Dokshitzer, M.H. Seymour and B.R. Webber, *Longitudinally invariant K_t clustering algorithms for hadron hadron collisions*, *Nucl. Phys. B* **406** (1993) 187.
- [66] S.D. Ellis and D.E. Soper, *Successive combination jet algorithm for hadron collisions*, *Phys. Rev. D* **48** (1993) 3160 [[hep-ph/9305266](#)].
- [67] M. Cacciari, G.P. Salam and G. Soyez, *The anti- k_t jet clustering algorithm*, *JHEP* **04** (2008) 063 [[0802.1189](#)].
- [68] T. Han, D. Liu, I. Low and X. Wang, *Electroweak couplings of the higgs boson at a multi-tev muon collider*, *Physical Review D* **103** (2021) .